

The Influence of Lamination Angles on the Interior Noise Levels of an Aircraft

Christian M. Fernholz

Ford Motor Company, Dearborn, MI

Jay H. Robinson

NASA Langley Research Center, Hampton, VA

Abstract

The feasibility of reducing the interior noise levels of an aircraft passenger cabin through an optimization of the composite lay up of the fuselage is investigated. MSC/NASTRAN, a commercially available finite element code, is used to perform the dynamic analysis and subsequent optimization of the fuselage. The numerical calculation of sensitivity of acoustic pressure to lamination angle is verified using a simple thin, cylindrical shell with point force excitations as noise sources. The thin shell is used because it represents a geometry similar to the fuselage and analytic solutions are available for the cylindrical thin shell equations of motion. Optimization of lamination angle for the reduction of interior noise is performed using a finite element model of an actual aircraft fuselage. The aircraft modeled for this study is the Beech Starship. Point forces simulate the structure borne noise produced by the engines and are applied to the fuselage at the wing mounting locations. These forces are the noise source for the optimization problem. The acoustic pressure response is reduced at a number of points in the fuselage and over a number of frequencies. The objective function, to be minimized, is the maximum sound pressure level at all response points in the passenger cabin and for all excitation frequencies in the range of interest.

Results from the study of the fuselage model indicate that a reduction in interior noise levels is possible over a finite frequency range through an optimal configuration of the lamination angles in the fuselage. Sound pressure level reductions of roughly 4 dB were attained at multiple locations in the passenger cabin. For frequencies outside the optimization range, the acoustic pressure response may increase after optimization. The effects of changing lamination angle on the overall structural integrity of the airframe are not considered in this study.

List of Symbols

A_{ij}, B_{ij}, D_{ij}	Stretching, bending-stretching coupling, and bending submatrices
B_s	Structural damping matrix
C	Fluid-structure coupling matrix
E	Young's modulus
F_{mn}	Amplitude of applied forces, modal formulation
F_o	Magnitude of applied forces
G	In-plane shear modulus
K_f, K_s	Fluid and structural stiffness matrices
M_f, M_s	Fluid and structural mass matrices
P_{mn}	Amplitude of acoustic pressure, modal solution
Q_{ij}	Local reduced stiffness matrix
\bar{Q}_{ij}	Global reduced stiffness matrix
U_{mn}	Amplitude of axial structural displacements, modal solution
V_{mn}	Amplitude of circumferential structural displacements, modal solution
W_{mn}	Amplitude of radial structural displacements, modal solution
a	Radius of the cylindrical shell
c_o	Acoustic speed of sound in air
h	Thickness of shell
i	$\sqrt{-1}$
k	Shell parameter $\frac{h^2}{12a^2}$
l	Length of the cylindrical shell
m	Axial modal coordinate
n	Circumferential modal coordinate
p	Acoustic pressure
P_{ref}	Acoustic reference pressure, 2.91×10^{-9} psi
r, θ, x	Cylindrical coordinate system
s	Non-dimensional shell axial coordinate $\frac{x}{a}$
t	Time

u, v, w	Axial, circumferential and radial structural displacements
x, y, z	Cartesian coordinate system
1, 2, 3	Material coordinate system
Φ_f, Φ_s	Uncoupled fluid and structure eigenvectors
γ	Structural damping coefficient
δ	Dirac delta function
η	Structural modal damping coefficient
λ_m	Non-dimensional modal parameter $\frac{m\pi a}{l}$
ν	Poisson's ratio
ξ_f, ξ_s	Fluid and structure modal amplitudes
ρ_f, ρ_s	Density of the fluid, structure
ψ	Lamination angle
ω	Frequency
Subscripts	
m, n	Axial and circumferential mode number
i, j	Matrix indices

Contents

Abstract	ii
List of Symbols	iii
Chapter 1 Introduction	1
Chapter 2 Theory and Methodology	5
Section 1 Finite Element Solution Methods	5
Section 2 Design Sensitivity and Optimization	8
Section 3 Optimization Problem for the Present Work	11
Chapter 3 The Thin, Cylindrical Shell	12
Section 1 The Specially Orthotropic Thin, Cylindrical Shell: Displacements and Pressures	13
Section 2 Analytical and Numerical Pressure Sensitivities to Composite Lamination Angle	16
Chapter 4 The Beech Starship	21
Section 1 The Finite Element Model of the Starship	22
Section 2 Formulation of the Optimization Problem for the Starship .	24
Section 3 Dynamic Analysis and Optimization of the Starship	25
Chapter 5 Conclusions	32
Chapter 6 Acknowledgments	35
Bibliography	36
Appendix A Equations of Motion for a Thin, Specially Orthotropic Cylindrical Shell	40
Appendix B Figures	46

Appendix C Sound Pressure Level at All Response Points for the
 Optimization Problem 62

Appendix D Computer Codes 69

 Section 1 FORTRAN Program compfreq.f 69

 Section 2 MathematicaTM program sensitivity.m 76

 Section 3 MSC/NASTRAN Bulk Data File 80

Chapter 1 Introduction

Since their design and development in the early 1960's, composite materials have played an increasingly important role in the design and construction of many different vehicles and structures [1]. As defined in Jones [2], a composite material consists of “two or more materials . . . combined on a macroscopic scale to form a useful material.” The material properties of composite materials are such that they generally have very favorable strength-to-weight and stiffness-to-weight ratios [2]. In many cases, the use of composite materials has substantially improved the performance of the structure over what could be attained using conventional materials. Not surprisingly, composite materials have found wide application in the construction of aircraft and spacecraft, vehicles for which performance is very sensitive to changes in weight.

Although the use of composite materials offers several advantages over conventional materials, several disadvantages are also apparent. From a design standpoint, one must be careful to account for the anisotropic characteristics typically displayed in composite materials. While a composite structure might have great strength in one direction, it may be structurally weak in another. Often times, it is possible to take advantage of anisotropic behavior and tailor a structure to meet a specific design requirement.

With the increasing use of composite materials in the construction of aircraft, interest has been expressed in reducing the interior sound pressure levels of passenger aircraft built from these materials. Work by Koval for a thin composite cylindrical shell [3] indicated that, from the perspective of noise reduction, use of composite materials in an aircraft fuselage may enable an aircraft designer to modify the transmission loss characteristics of the fuselage to meet a specific noise requirement. In a noise reduction example for a composite shell from this work, the author discussed the possibility of

using the lamination angles to attenuate noise transmission through the structure over a specific frequency range. However, less satisfactory acoustic characteristics for the shell may result in other frequency ranges and would have to be addressed using conventional sound proofing measures.

Aircraft fuselages have been modeled as thin, cylindrical shells as a means of understanding the coupling of the structural vibration modes to the acoustic modes in the fuselage interior [4]. The thin, cylindrical shell has been used because an analytic solution describing its motion can be derived. The same is not true for most aircraft structures.

Salagame *et al.* [5] developed analytical expressions for the sensitivity of the acoustic power emitted by a vibrating flat plate to a change in one of the design variables of the plate. These analytical sensitivities were compared to a numerical optimization to reduce the acoustic power radiated by a clamped, isotropic plate through an optimal thickness distribution through the plate. This work demonstrated the feasibility of using acoustic sensitivities to structural attributes in a noise reduction optimization.

Lamancusa [6] discusses many different objective function formulations for the reduction of radiated noise from a clamped, isotropic plate in which thickness is allowed to vary. In this work, the author develops objective functions based on various acoustic measures such as radiated sound power, mean-square velocity, and modal radiation efficiency. The importance of proper objective function, design constraints, and design variables is discussed in this work. A poorly specified optimization problem can make it difficult to attain convergence to a global optimum with an optimization algorithm. In a slightly different approach, Naghshineh *et al.* [7] first specified a minimum radiation condition for a beam radiating in a rigid baffle. Then, an optimal distribution of Young's modulus and density for the beam was found to force the beam to vibrate in the minimum

radiation mode.

Recent research has been undertaken to structurally optimize the thickness distribution of an isotropic cylindrical shell for the purpose of minimizing the interior noise levels [8, 9]. Noise levels for a single excitation frequency were successfully reduced through the generation of an optimum thickness distribution around and along the cylindrical shell. In this work, the authors noted a strong dependence of the final optimum solution on the starting values of the design variables of the problem.

For cylindrical shells made from laminated composite materials, considerable work has been done in the study of the optimization of lamination angle to maximize the buckling strength. The work of Rao [10] and the work of Hu [11] each demonstrated the ability to increase the buckling pressure of a thin, cylindrical shell through an optimization of angle for a variety of boundary conditions. Many composite cylinder buckling studies, including those of Hu, have been undertaken through the use of the finite element method.

MSC/NASTRAN¹, a commercially available computer code, has been used as a tool for the prediction of aircraft interior noise in a number of earlier studies [13, 14]. However, these studies have used the so-called structural-acoustic analogy [15] as a means of calculating the acoustic pressure response of the fluid. Recent upgrades to the MSC/NASTRAN computer code allow the user to model the fluid and compute acoustic responses directly. Work by Fernholz *et al.* [16] demonstrated the feasibility of using a fully-coupled fluid/structure analysis for a cylindrical model. More importantly to the current work, this feature makes it feasible to optimize the model using acoustic responses as design variables or objectives.

The objective of the present study is to demonstrate the feasibility of sound pressure level reduction through an optimal lamination angle configuration in a composite aircraft

¹ NASTRAN is an acronym standing for NASA STRuctural ANalysis [12].

fuselage. To achieve this reduction, the lamination angles in the fuselage are optimized over a range of excitation frequencies. Unlike previous studies, the geometry of an actual aircraft, rather than a cylindrical shell, is used in the optimization analysis. The aircraft used is the Beech Starship, an eight- to ten-person twin turboprop aircraft. The Starship is modeled and analyzed using the finite element method. Loads simulating the structure-borne noise produced by the engines are applied to the model. MSC/NASTRAN is used to perform the finite element analysis and subsequent lamination angle optimization. The effects of changing lamination angle on the overall structural integrity of the airframe are not considered in this study.

This study is divided into five chapters. The methodology and theory of the finite element solution method and ply-angle optimization is outlined in Chapter 2. In Chapter 3, this methodology is applied to a thin, orthotropic cylindrical shell. Analytical solutions for the motion of the cylinder are given. The numerical solutions and design sensitivities are compared with analytical solutions from classical thin shell theory. In Chapter 4, the methodology developed in Chapter 2 is applied to the Beech Starship fuselage. Because an analytical solution for the motion of the fuselage is not available, only a numerical analysis is performed. Finally, Chapter 5 contains a discussion of the results of this work. Appendices include a derivation of a solution to the Donnell-Mushtari equations of motion for a thin cylindrical shell composed of specially orthotropic materials, figures related to the current work, and complete output data for all the response locations used in this study.

Chapter 2 Theory and Methodology

Because of the complexity of the aircraft fuselage and interior fluid system, much of this work was necessarily dependent upon numerical methods of analysis. In particular, a fully-coupled finite element method was used to model both the aircraft structure and the air inside the passenger cabin. MSC/NASTRAN, the computer code used to perform the finite element analysis, was also used to optimize the lamination angles of the fuselage composite material for the reduction of the aircraft interior noise levels.

In this chapter, methods of solving a finite element problem for a system containing both fluid and structural components are outlined. As the finite element modeling method is quite common and well understood, only the solution methods are provided here. For more detail regarding finite element theory, the reader is referred to the literature [12, 17, 18].

Less common in standard engineering practice, but more critical to this particular work, is design sensitivity and optimization. Therefore, more of this chapter is devoted to understanding these methods than to finite element analysis. In particular, close attention is given to the specification of the objective function and constraints within MSC/NASTRAN.

2.1: Finite Element Solution Methods

The equation of motion for a structure for the eigenvalue problem is written as [18]

$$[M_s]\{\ddot{u}\} + [K_s]\{u\} = 0 \quad (1)$$

where $[K_s]$ represents the stiffness matrix of the structure, $[M_s]$ the mass matrix, and $\{u\}$ the displacement vector for the structural element nodes. Assuming a harmonic solution

for $\{u\}$, Equation (1) becomes

$$([K_s] - \lambda[M_s])\{\Phi_s\} = 0 \quad (2)$$

where $\{\Phi_s\}$ represents the structural eigenvectors of the system. The eigenvalues λ of the problem are related to the natural frequencies through

$$\lambda = \omega_n^2 \quad (3)$$

where ω_n represents the natural frequencies of vibration in rad/sec [19]. For this work, the Lanczos method was used to calculate the eigenvalues of the system because it usually represents the best solution method for problems having a large number of degrees of freedom [19].

For a frequency response analysis, the equation of motion of the structure is written as [18]

$$[M_s]\{\ddot{u}\} + [B_s]\{\dot{u}\} + [K_s]\{u\} = e^{i\omega t}[F(\omega)] \quad (4)$$

where the $F(\omega)$ represents a harmonic excitation to the structure and $[B_s]$ represents the damping matrix for the structure. If a steady-state harmonic solution is assumed, Equation (4) becomes

$$(-\omega^2[M_s] + i\omega[B_s] + [K_s])\{u(\omega)\} = [F(\omega)] \quad (5)$$

Here, ω represents the excitation frequency of the system.

Fluids are modeled using three-dimensional elements having one degree of freedom at each node, that degree of freedom being the acoustic pressure. The equation of motion for the frequency response analysis of the fluid is [20]

$$[M_f]\{\ddot{p}\} + [K_f]\{p\} + \rho_f[C]\{\ddot{u}\} = [0] \quad (6)$$

where $[M_f]$ is the acoustic “mass” matrix and $[K_f]$ the acoustic “stiffness” matrix. The $[C]$ matrix couples the motion of the structure to the acoustic pressure in the fluid. At the fluid-structure interface, the boundary condition for the fluid is

$$\frac{\partial p}{\partial n} = -\rho_f \frac{\partial^2 u_n}{\partial t^2} \quad (7)$$

where n is the unit outward normal vector to the surface of the structure, ρ_f is the density of the fluid, and u_n is the displacement of the structure in the normal direction. This boundary condition is reflected in the third term of Equation (6). The fluid in turn affects the motion of the structure by applying forces over the structural surface area of [21]

$$\{F_p\} = -[C^T]\{p\} \quad (8)$$

The coupled equations of motion for the fluid and structure are thus [21]

$$\begin{bmatrix} M_s & 0 \\ \rho_f C & M_f \end{bmatrix} \begin{Bmatrix} \ddot{u} \\ \ddot{p} \end{Bmatrix} + \begin{bmatrix} B_s & 0 \\ 0 & 0 \end{bmatrix} \begin{Bmatrix} \dot{u} \\ \dot{p} \end{Bmatrix} + \begin{bmatrix} K_s & -C^T \\ 0 & K_f \end{bmatrix} \begin{Bmatrix} u \\ p \end{Bmatrix} = e^{i\omega t} \begin{Bmatrix} F(\omega) \\ 0 \end{Bmatrix} \quad (9)$$

Two methods of solution can be used to solve the frequency response problem. The direct method essentially solves Equation (9) as shown for discrete excitation frequencies [19]. This method, while generally accurate for a wide variety of structural configurations, can be computationally expensive, particularly for a large number of excitation frequencies.

The second method that can be used to solve the frequency response problem is the modal method. In this method, the physical variables of the problem (p, u) are assumed to be a linear combination of the uncoupled acoustic and structural modes

$$\begin{aligned} [u] &\approx [\Phi_s][\xi_s(\omega)]e^{i\omega t} \\ [p] &\approx [\Phi_f][\xi_f(\omega)]e^{i\omega t} \end{aligned} \quad (10)$$

where Φ_s are the uncoupled eigenvectors of the structure, Φ_f the uncoupled eigenvectors of the fluid, and ξ_s and ξ_f are the modal amplitudes for the structure and fluid respectively.

Note that Equation (10) becomes an equality if all the modes of the system are used [19]. However, this is typically not done. Substituting this relation into Equation (9) and pre-multiplying by the transposed transformation matrix yields [20]

$$\begin{bmatrix} \Phi_s^T M_s \Phi_s & 0 \\ \rho_f \Phi_f^T A \Phi_s & \Phi_f^T M_f \Phi_f \end{bmatrix} \begin{Bmatrix} \ddot{\xi}_s \\ \ddot{\xi}_f \end{Bmatrix} + \begin{bmatrix} \Phi_s^T B_s \Phi_s & 0 \\ 0 & 0 \end{bmatrix} \begin{Bmatrix} \dot{\xi}_s \\ \dot{\xi}_f \end{Bmatrix} + \begin{bmatrix} \Phi_s^T K_s \Phi_s & -\Phi_s^T A^T \Phi_f \\ 0 & \Phi_f^T K_f \Phi_f \end{bmatrix} \begin{Bmatrix} \xi_s \\ \xi_f \end{Bmatrix} = \begin{Bmatrix} \Phi_s^T F(\omega) \\ 0 \end{Bmatrix} \quad (11)$$

This system of equations is solved in using the direct frequency approach described above. The number of modes used in this solution is usually much less than the number of physical variables in the system and the use of this method can represent a substantial computational savings over the direct method [19]. However, a modal truncation error is also associated with this method. Care must be taken to ensure that a sufficient number of modes are used to reduce the truncation error to an acceptable level.

2.2: Design Sensitivity and Optimization

In general, design sensitivity is the change of a structural or system response with respect to changes in a design variable. Design optimization is the process of generating improved designs subject to certain constraints and criteria [22]. Sensitivity analysis and design optimization are closely related, particularly in computer implementations, as the responses computed in the sensitivity analysis can be used in the optimization algorithm to determine the search direction for the objective function.

The ij -th design sensitivity coefficient λ_{ij} is defined as

$$\lambda_{ij} = \left. \frac{\partial r_j}{\partial x_i} \right|_{\vec{x}_o} \quad (12)$$

where r_j is the j -th response and x_i is the i -th design variable. The sensitivity coefficient is calculated for the \vec{x}_o vector of design variables [22].

The following components are included in the basic statement of a design optimization problem [23]:

Objective Function

Minimize $F(\vec{x})$ subject to

Inequality Constraints

$$g_j(\vec{x}) \leq 0 \quad j = 1, 2, \dots, n_g$$

Equality Constraints

$$h_k(\vec{x}) = 0 \quad k = 1, 2, \dots, n_h$$

Side Constraints

$$x_i^l \leq x_i \leq x_i^u \quad i = 1, 2, \dots, n \text{ where}$$

Design Variables

$$\vec{x} = \{x_1, x_2, \dots, x_n\}$$

Here, the objective function represents the attribute of the system which the user is trying to minimize. The design variables are the components of the model which the user can change in order to minimize the value of the objective function. The equality and inequality constraints limit the values that the objective function can assume. That is, they limit the range over which the user can search for an optimum value for the objective function. Likewise, the side constraints limit the values of the design variables for the problem.

In a design optimization problem, the MSC/NASTRAN optimizer uses the design sensitivity and objective function gradients to locate a global objective function minimum. When no constraints are active or violated, the Method of Steepest Descent is used [22]. However, this method is not particularly robust and there is often difficulty in converging to an optimum value when using the Method of Steepest Descent. Thus, on subsequent iterations, or for design cycles in which constraints are active or violated, the Modified Method of Feasible Directions is used. With this method, one of the constraints is

followed until a global optimum for the objective function is found. During the process of finding this value, some of the constraints for the problem can be slightly violated [22]. For more information regarding these methods, the reader is referred to the literature [22, 23, 24].

The MSC/NASTRAN design cycle flow is as shown in Figure B1. At the start of each cycle, a full finite element analysis of the model is performed. The finite element data is then used to develop an approximate representation of the model. The approximate model is constructed using first-order Taylor Series expansions for the responses in the system [22]. This approximate model is used for the calculation of the design sensitivities and constraints for the current design cycle. Furthermore, the approximate model contains a reduced number of constraints which in turn improves the efficiency of the optimizer calculation [22]. Next, a check for hard convergence is performed and, if satisfied, the optimization algorithm exits. If the conditions for hard convergence are not satisfied, the optimizer performs an optimization using the data in the approximate model. After completion of optimization, the optimizer checks for soft convergence. If the criteria for soft convergence are satisfied, the optimizer exits. If not, the model is updated based on the results of the optimization and a finite element analysis of the model is performed to begin the next design cycle [24].

Convergence with the MSC/NASTRAN optimizer can be attained in a number of ways. First, hard convergence can be attained if the Kuhn-Tucker conditions are satisfied. Satisfaction of these conditions indicates that a local optimum value for the objective function has been reached. Hard convergence can also be attained if the maximum number of design cycles for the optimizer is reached, or if no feasible solution for the optimization problem exists. Soft convergence is attained if the absolute or the relative change in the value of the objective function is less than some minimum value from one

design cycle to the next [22].

2.3: Optimization Problem for the Present Work

It was desired to reduce the noise levels inside the aircraft below an initial, baseline pressure at a number of response locations and for a number of excitation frequencies. To accomplish this, the objective function was chosen to represent the maximum acoustic response for the set of response locations over a range of excitation frequencies specified for the problem. The value of the objective function was then minimized at all response points in the cabin and for all excitation frequencies in the range of interest. Mathematically, the optimization problem can be written

Minimize OBJ with

$$\text{OBJ}(\psi_k) = \max_{j,\omega} \left\{ 10 \log_{10} \left(\frac{|p_j(\psi_k)|^2}{p_{ref}^2} \right) \right\} \quad \text{where} \quad (13)$$

$$\psi = \{\psi_1, \psi_2, \dots, \psi_k\} \quad (14)$$

where the design variables for the problem, ψ_k^2 , represented the composite lamination angles and OBJ represented the maximum sound pressure level at the j response locations in the problem over the range of frequencies ω .

The objective function was specified in this manner so that the sound pressure level at several excitation frequencies could be reduced. Had the objective function been formulated to reduce the acoustic pressure response directly, it would have been feasible to do so only for a single frequency. However, by setting the objective function equal to the maximum response in a set of locations and frequencies, the sound pressure levels at several frequencies were included as a design response and included within the optimization calculation (see Figure B2).

² The lamination angles for composite material lamina are commonly denoted in the literature (e.g. Jones [2]) by the Greek letter θ . However, this work uses θ as the circumferential coordinate in the cylindrical coordinate system. To avoid confusion, ψ was chosen to represent lamination angle.

Chapter 3 The Thin, Cylindrical Shell

Before applying the methodology described in Chapter 2 to the Beech Starship fuselage, this analysis was applied to a thin, cylindrical shell. The thin cylindrical shell shares some geometric similarities with the fuselage, but, unlike the fuselage, it is possible to write closed form solutions to the equations of motion of the cylinder. These solutions are used to ascertain the extent of the modal truncation errors in the numerical modal solution and as a check on the numerical design sensitivity calculations for the optimization problem.

The Donnell-Mushtari theory is applied to a thin, open, circular cylinder having dimensions similar to those of the Starship passenger cabin section and composed of a single-layer, specially orthotropic material. A cylindrical coordinate system is used to describe the model with the origin located at the center of one of the open ends of the cylinder. The positive x-axis is located along the axis of the cylinder. The ends of the cylinder are simply supported in the circumferential and radial directions and are unsupported in the axial direction. Structural endcaps are not included in the model. Boundary conditions of $p=0$ are applied to the fluid at the open faces at each end of the cylinder. Two harmonic, in-phase point forces of equal magnitude are applied to the cylinder. The forces are located 180° apart circumferentially and at one-half the length of the cylinder axially. The radial motion of the cylinder is coupled to the motion of the fluid inside the cylinder and an analytical relation describing the acoustic pressure at any point in the fluid is derived. Numerical modal and direct solutions are compared to the analytical solution.

The last analysis performed on the composite cylinder is a sensitivity analysis of the acoustic pressure response of the fluid inside the shell with respect to ply angle for angles

near zero degrees. To determine this sensitivity analytically, it is necessary to use the cylindrical equations of motion for a generally orthotropic material. To include the effect lamination angle has on bending terms in the equations of motion, it is also necessary to use the Love-Timoshenko equations for the motion of a thin shell. A solution for the generally orthotropic material is not developed. However, for lamination angles of zero degrees, the generally orthotropic material becomes specially orthotropic, and the solution developed for those materials can be used to find the sensitivity of pressure to lamination angle. Comparison of the numerical sensitivity to the analytical sensitivity is made, and a difference between the two solutions is manifested.

3.1: The Specially Orthotropic Thin, Cylindrical Shell: Displacements and Pressures

As shown in Appendix A, a solution for the specially orthotropic thin cylindrical shell equations of motion can be written

$$\begin{aligned}
 u(\theta, x, t) &= e^{i\omega t} \sum_{m=0}^{\infty} \sum_{n=0}^{\infty} U_{mn} \cos(\lambda_m s) \cos(n\theta) \\
 v(\theta, x, t) &= e^{i\omega t} \sum_{m=1}^{\infty} \sum_{n=0}^{\infty} V_{mn} \sin(\lambda_m s) \sin(n\theta) \\
 w(\theta, x, t) &= e^{i\omega t} \sum_{m=1}^{\infty} \sum_{n=0}^{\infty} W_{mn} \sin(\lambda_m s) \cos(n\theta)
 \end{aligned} \tag{15}$$

where u , v , and w represent the axial, circumferential, and radial displacements of the shell.

The acoustic pressure at any point in the fluid within the shell is given as

$$p(r, \theta, x, t) = e^{i\omega t} \sum_{m=1}^{\infty} \sum_{n=1}^{\infty} P_{mn} J_n(\alpha_m r) \sin(\lambda_m s) \cos(n\theta) \tag{16}$$

In the derivation for the acoustic pressure within the shell, a partially-coupled solution between the structure and the fluid has been assumed. The structure influences the behavior of the fluid, but not vice versa. In MSC/NASTRAN, a fully-coupled response

is computed. For most aircraft-type structures, the back-pressure forces on the structure can be neglected [25]. An exploded view of the fluid-structure problem as formulated above for the thin cylindrical shell filled with air is shown in Figure B3. Also shown are the applied forces for this problem.

The finite element model was constructed using quadratic quadrilateral elements with 2464 nodes for the structure and quadratic pentahedral elements with 20,501 nodes for the fluid. The structural elements had five degrees of freedom at each node (three displacements and two rotations) and the fluid elements had one degree of freedom (pressure) at each node. The fluid and structure nodes were matched one-to-one on the surfaces where they were in contact. For the structural elements in the model, a structural damping value of 1% of critical was applied while the fluid elements remained undamped. This finite element model is shown in figure B4.

A comparison of the analytical and numerical frequency responses is shown in Figures B5, B6, B7, and B8. Figure B5 shows the numerical modal solution calculated using MSC/NASTRAN for the radial displacement of a point on the shell verses the excitation frequency of the applied forces. Also shown in this figure is the analytical solution derived in Appendix A. The numerical solution used 1000 structural vibration modes in a range from 0.0 Hz to 499.67 Hz to compute the structural response. For comparison, the analytic solution used 1600 modes. This range of frequencies was chosen to ensure that a sufficient number of modes were specified for the excitation frequency range of interest (1.0 to 150.0 Hz). In general, there is good agreement between the analytical and numerical models for the cylinder. There are several reasons why the agreement between the two responses is not as close at the higher frequencies of the range shown. First, the number of elements in the model may be insufficient to capture the higher-order mode shapes of the response. Secondly, different shell theories are used for the numerical and

analytical solutions and the analytical model is partially-coupled, while the numerical model is fully-coupled. Also, some of the differences in the response amplitudes may be attributable to the moderately light damping which was applied.

The comparison between the analytical and numerical solutions for sound pressure level at a point in the fluid is shown in Figure B6. A total of 300 fluid modes over a range of 41.52 Hz to 627.2 Hz were used in the numerical solution to represent the fluid response. As was the case for the structural response, this range was chosen to minimize the modal truncation error for the excitation frequency range of interest. The major response peaks of the system are captured by both methods. However, a discrepancy between the two solutions is apparent at approximately 105 Hz. The analytical solution shows a response peak in this region, but there is no corresponding peak in the numerical solution. Likewise there are substantial differences between the two solutions in the amplitudes of the first two response peaks. These differences can again be attributed to the reasons outlined above for the solutions for the structural displacement.

Figures B7 and B8 show a similar comparison for the same model. For these figures, the numerical direct frequency response is plotted versus excitation frequency. The direct response was computed for two smaller frequency ranges, one from 20 to 60 Hz and the other from 90 to 110 Hz. This was done because a direct frequency response is computationally more expensive than a modal solution, particularly if the model has a large number of degrees of freedom, or if responses for a number of excitation frequencies are desired. The first frequency range, 20 to 60 Hz, was chosen to see how well the numerical solution would resolve the fluid response near 41 Hz. The second frequency range, 90 to 110 Hz, was chosen to compare the analytical and numerical solutions for the anti-resonance at approximately 100 Hz.

From Figure B7, a close agreement between the analytical and numerical finite

element solutions is again apparent. Both solutions capture the vibration characteristics of the structure over the range of excitation frequencies. There are slight differences between the two solutions, again attributable to differences in the shell theories used for each solution method. Figure B8 shows the acoustic response for a point in the fluid interior to the shell. A close agreement is noted between the analytical and numerical direct solutions.

From an analysis of these models, it can be concluded that the numerical solutions calculated using the finite element method provides a solution very close to that predicted by analytical models, particularly for the structural portions of the system. However, care must be exercised when using the modal solution method. One must ensure that modal truncation errors have been minimized, or at least reduced to an acceptable level. As a check on the modal solution for cases where an analytical solution is not available, it may be advisable to run a direct solution over the frequency range of interest.

3.2: Analytical and Numerical Pressure Sensitivities to Composite Lamination Angle

The shell equations of motion for a single-layer, generally orthotropic material were used to develop an analytical model of the sensitivity of acoustic pressure to lamination angle. To account for the effect lamination angle has on the bending terms in the equations of motion, the Love-Timoshenko equations were used. A general solution for the generally orthotropic equations was not developed, but for a lamination angle of zero degrees, the shell material becomes specially orthotropic, and the solution developed in Appendix A for specially orthotropic materials can be used. This solution was used to calculate the sensitivity of the acoustic pressure to a change in lamination angle at zero

degrees. Through comparison to Equation (12), we see that we are essentially calculating

$$\lambda = \left. \frac{\partial p}{\partial \psi} \right|_{\psi=0^\circ} \quad (17)$$

If this quantity is positive, then the acoustic response inside the shell will increase as the lamination angle is changed from zero degrees.

The Love-Timoshenko equations of motion for a single-layer generally orthotropic thin cylindrical shell can be written [29, 26]

$$\begin{bmatrix} L_{11} & L_{12} & L_{13} \\ L_{21} & L_{22} & L_{23} \\ L_{31} & L_{32} & L_{33} \end{bmatrix} \begin{bmatrix} u \\ v \\ w \end{bmatrix} = \frac{1}{A_{22}} \begin{bmatrix} f_x \\ f_\theta \\ f_r \end{bmatrix} \quad (18)$$

where

$$\begin{aligned} L_{11} &= \frac{A_{11}}{A_{22}} \frac{\partial^2}{\partial s^2} + 2 \frac{A_{16}}{A_{22}} \frac{\partial^2}{\partial s \partial \theta} + \frac{A_{66}}{A_{22}} \frac{\partial^2}{\partial \theta^2} - \frac{\rho h a^2}{A_{22}} \frac{\partial^2}{\partial t^2} \\ L_{12} &= \frac{A_{16}}{A_{22}} \frac{\partial^2}{\partial s^2} + \frac{A_{12} + A_{66}}{A_{22}} \frac{\partial^2}{\partial s \partial \theta} + \frac{A_{26}}{A_{22}} \frac{\partial^2}{\partial \theta^2} \\ L_{13} &= \frac{A_{26}}{A_{22}} \frac{\partial}{\partial \theta} + \frac{A_{12}}{A_{22}} \frac{\partial}{\partial s} \\ L_{21} &= \frac{A_{16}}{A_{22}} \frac{\partial^2}{\partial s^2} + \frac{A_{12} + A_{66}}{A_{22}} \frac{\partial^2}{\partial s \partial \theta} + \frac{A_{26}}{A_{22}} \frac{\partial^2}{\partial \theta^2} \\ L_{22} &= \frac{A_{66}}{A_{22}} \frac{\partial^2}{\partial s^2} + 2 \frac{A_{26}}{A_{22}} \frac{\partial^2}{\partial s \partial \theta} + k \left[2 \frac{D_{66}}{D_{22}} \frac{\partial^2}{\partial s^2} + 3 \frac{D_{26}}{D_{22}} \frac{\partial^2}{\partial s \partial \theta} + 2 \frac{\partial^2}{\partial \theta^2} \right] - \frac{\rho h a^2}{A_{22}} \frac{\partial^2}{\partial t^2} \\ L_{23} &= \frac{A_{26}}{A_{22}} \frac{\partial}{\partial s} + \frac{\partial}{\partial \theta} + k \left[\frac{D_{16}}{D_{22}} \frac{\partial^3}{\partial s^3} - \left(\frac{D_{12} + 2D_{66}}{D_{22}} \right) \frac{\partial^3}{\partial s^2 \partial \theta} - 3 \frac{D_{26}}{D_{22}} \frac{\partial^3}{\partial s \partial \theta^2} - \frac{\partial^3}{\partial \theta^3} \right] \\ L_{31} &= \frac{A_{26}}{A_{22}} \frac{\partial}{\partial \theta} + \frac{A_{12}}{A_{22}} \frac{\partial}{\partial s} \\ L_{32} &= \frac{A_{26}}{A_{22}} \frac{\partial}{\partial s} + \frac{\partial}{\partial \theta} + k \left[-2 \frac{D_{16}}{D_{22}} \frac{\partial^3}{\partial s^3} - \left(\frac{D_{12} + 4D_{66}}{D_{22}} \right) \frac{\partial^3}{\partial s^2 \partial \theta} - 4 \frac{D_{26}}{D_{22}} \frac{\partial^3}{\partial s \partial \theta^2} - \frac{\partial^3}{\partial \theta^3} \right] \\ L_{33} &= 1 + k \left[\frac{D_{11}}{D_{22}} \frac{\partial^4}{\partial s^4} + 2 \left(\frac{D_{12} + 2D_{66}}{D_{22}} \right) \frac{\partial^4}{\partial s^2 \partial \theta^2} + \frac{\partial^4}{\partial \theta^4} + 4 \frac{D_{16}}{D_{22}} \frac{\partial^4}{\partial s^3 \partial \theta} + 4 \frac{D_{26}}{D_{22}} \frac{\partial^4}{\partial s \partial \theta^3} \right] \\ &\quad + \frac{\rho h a^2}{A_{22}} \frac{\partial^2}{\partial t^2} \end{aligned} \quad (19)$$

and

$$\begin{aligned}
A_{ij} &= \int_{-\frac{h}{2}}^{\frac{h}{2}} \bar{Q}_{ij} d\xi \\
B_{ij} &= \int_{-\frac{h}{2}}^{\frac{h}{2}} \bar{Q}_{ij} \xi d\xi \\
D_{ij} &= \int_{-\frac{h}{2}}^{\frac{h}{2}} \bar{Q}_{ij} \xi^2 d\xi
\end{aligned} \tag{20}$$

h represents the lamina thickness, $s = \frac{x}{a}$, $k = \frac{h^2}{12a^2}$, and \bar{Q}_{ij} represents the ij —th reduced stiffness in the global coordinate system. The A_{ij} , B_{ij} , and D_{ij} terms are commonly denoted in the literature [26] as the stretching, bending-stretching coupling, and bending submatrices, respectively. The B_{ij} submatrix has been included here for completeness. For a single-layer laminate, such as the cylinder used in this chapter, the B_{ij} submatrix becomes zero.

The principal material axes of an orthotropic material are not, in general, aligned with the natural body axes of a given problem (see Figure B9). The lamination angle ψ relates the reduced stiffnesses in the global coordinate system to the stiffnesses in the material coordinate system. These relations are written [2]

$$\begin{aligned}
\bar{Q}_{11} &= Q_{11} \cos^4 \psi + 2(Q_{12} + 2Q_{66}) \sin^2 \psi \cos^2 \psi + Q_{22} \sin^4 \psi \\
\bar{Q}_{12} &= (Q_{11} + Q_{22} - 4Q_{66}) \sin^2 \psi \cos^2 \psi + Q_{12}(\sin^4 \psi + \cos^4 \psi) \\
\bar{Q}_{22} &= Q_{11} \sin^4 \psi + 2(Q_{12} + 2Q_{66}) \sin^2 \psi \cos^2 \psi + Q_{22} \cos^4 \psi \\
\bar{Q}_{16} &= (Q_{11} - Q_{12} - 2Q_{66}) \sin \psi \cos^3 \psi + (Q_{12} - Q_{22} + 2Q_{66}) \sin^3 \psi \cos \psi \\
\bar{Q}_{26} &= (Q_{11} - Q_{12} - 2Q_{66}) \sin^3 \psi \cos \psi + (Q_{12} - Q_{22} + 2Q_{66}) \sin \psi \cos^3 \psi \\
\bar{Q}_{66} &= (Q_{11} + Q_{22} - 2Q_{12} - 2Q_{66}) \sin^2 \psi \cos^2 \psi + Q_{66}(\sin^4 \psi + \cos^4 \psi)
\end{aligned} \tag{21}$$

where the bar over the Q_{ij} indicates that the reduced stiffnesses have been transformed to the global coordinate system. The angle ψ represents the angle between the global

x-axis and the local 1-axis, measured counter clockwise from the x-axis [27]. Note that for $\psi=0^\circ$ and $\psi=90^\circ$, the material becomes specially orthotropic.

Figure B10 shows a comparison between analytical and numerical solutions of $\frac{\partial p}{\partial \psi}$ versus frequency for $\psi=0^\circ$ in the thin, cylindrical shell. For this case, the numerical solution is a direct frequency response. Figures B11 and B12 show the analytical radial displacement of the shell and the acoustic pressure response of the fluid respectively at the same location as the sensitivity shown in Figure B10. Each of these figures shows a response over the frequency range 20 to 50 Hz. The range of excitation frequencies was chosen because it contained both structural and acoustic resonances.

From these figures, it is evident that the greatest sensitivity of acoustic pressure to lamination angle is displayed in the vicinity of the resonant peaks of the system. For this frequency range, the resonant responses occur at approximately 24.70 Hz (structural mode 1,6), 32.05 Hz (structural mode 1,4), 41.52 Hz (fluid mode 1,0,1), and 47.58 Hz (structural mode 1,10)³. There is good agreement between the analytical and numerical sensitivities. In particular, the peaks in the sensitivities occur at roughly the same frequencies and the signs of the sensitivities are the same between the solutions. To simplify the analytical solution, damping was not applied to either the numerical or the analytical solutions. The absence of damping is likely the cause of the difference in the sensitivity amplitudes.

A difference between the analytical and numerical solutions is apparent near the acoustic peak in the response. The numerical solution for acoustic pressure sensitivity shows a sensitivity to lamination angle near this peak, while the analytical solution does not. This is attributable to the different assumptions that were made for each solution. In the analytical solution, only one structural mode couples to each acoustic

³ For structural mode shapes, the first number indicates the order of the axial component of the mode and the second number indicates the order of the circumferential component of the mode. For fluid mode shapes, the first number corresponds to the radial order of the mode, the second to the circumferential order, and the third number indicates the axial order of the mode.

mode as the fluid and structural modes are assumed to be orthogonal. This assumption is enforced even for the generally orthotropic material. The influence of the structural mode associated with the fluid resonance near 41 Hz is very slight. Thus, the sensitivity of that response to lamination angle will likewise be very small. In the numerical solution for the generally orthotropic material, the fluid and structure modes are no longer orthogonal and the modal amplitudes of a number of structural modes, rather than a single mode, can be quite substantial for the acoustic peaks of the response. Thus, the sensitivity of acoustic pressure to lamination angle will likewise be larger in the numerical solution. This difference points out some of the limitations of the analytical solution used for this analysis. In general, there is a good correlation between the analytical solutions and the numerical solutions calculated using MSC/NASTRAN. In particular, the calculation of sensitivity of acoustic pressure to lamination angle appears valid and can be used for the optimization of the Starship fuselage.

Chapter 4 The Beech Starship

The primary aim of this work is the demonstration of the feasibility of reducing the noise levels in the interior of an actual aircraft fuselage through the optimization of the lamination angles in the aircraft fuselage. The Beech Starship is the aircraft used for this study. The Starship fuselage and passenger cabin interior is modeled and analyzed using the finite element method. Because this work is concerned with the acoustics of the fuselage interior, no attempt was made to model the wings of the aircraft.

In this chapter, the optimization problem for the fuselage is formulated to reduce the acoustic pressure at a number of response points in the cabin interior and over a range of excitation frequencies. The objective function is minimized with the constraint that it be greater than the acoustic pressure at the response locations. The fuselage lamination angles are used as the optimization design variables.

Point forces are applied to the fuselage at the wing mounting locations. These forces represent the structure-borne noise in the aircraft produced by the engines and they are the noise source for the optimization problem.

It was desired to use the modal frequency response solution for the present work because a substantial time savings is typically associated with the use of this method over the use of the direct method. A preliminary modal frequency analysis is performed on the model and, to ascertain the extent of the modal truncation error associated with this model, a direct frequency response analysis is performed over the range of the optimization frequencies.

The results of the optimization of lamination angle for the reduction of interior noise are next discussed. The design cycle histories for the objective function and design variables are charted. A modal frequency analysis using the final lamination angles

calculated by the optimization algorithm is used to measure the decrease in interior sound pressure level.

4.1: The Finite Element Model of the Starship

The Beech Starship is an eight- to ten-passenger twin turboprop aircraft designed and developed in the early 1980's by the Beech aircraft company [30]. It is a unique aircraft in many respects. The main wing is located on the aft section of the aircraft, with two smaller canards in front. These canards pivot automatically with the main wing flaps to maintain pitch and trim [30]. The two engines are mounted on the main wing in a "pusher" configuration. Lastly, much of the aircraft structure is constructed from composite materials.

Using data provided by the Raytheon Aircraft Company, the NASA Langley Research Center developed a geometric representation of the Starship. Included in this representation were the passenger cabin windows, the cockpit windows, passenger cabin door, and the aircraft emergency escape hatch. Because the present work concerned the acoustics of the aircraft cabin no attempt was made to model the wings of the Starship. An isometric view of the geometric model of the Starship is shown in Figure B13. The Cartesian coordinate system used for the analysis of the Starship is also shown in this figure for reference. More detail regarding this system and the location of the origin for the problem is contained in Appendix C.

This geometric model was used for the generation of both the structural and fluid finite element meshes. Like the geometric model, the finite element models for this study were constructed by the NASA Langley Research Center. The structure of the fuselage was modeled using several different element types. Most of the aircraft, including the fuselage and windows, was modeled with quadratic quadrilateral elements. The nose

of the aircraft was modeled with quadratic trilateral elements. Stringers and stiffeners present in the Starship were modeled using beam elements. These beams were used primarily as reinforcement around the windows and doors of the aircraft. A total of 10,620 nodes, each having five degrees of freedom, were used to model the Starship structure. An isometric view of the structural finite element mesh is shown in Figure B14. Figure B15 shows the location of the beam elements in the model.

The final aspect of the Starship which was modeled was the air inside the passenger cabin. This was the only region of the aircraft where the fluid was modeled. Similar fluid models were not created for the cockpit or baggage sections of the aircraft. The air within the passenger section was modeled using linear tetrahedral elements and 6887 nodes. Each of the fluid nodes had one degree of freedom. Linear elements were used in the fluid to ensure proper coupling to the structure at the fluid-structure interfaces of the model. An isometric view of the fluid portion of the Starship model is shown in Figure B16. In the complete model, the aircraft structural finite element mesh enclosed the finite element mesh of the fluid. On the surfaces where the two were in contact, the fluid nodes were each matched to a structural node. No structural details of the passenger cabin interior were modeled. Therefore, this section of the model did not include interior trim panels or a floor.

Most of the fuselage is constructed from a single section of sandwich composite material. The middle layer of this composite is a 0.75"-thick honeycomb core. Four graphite epoxy face sheets, each between 0.0085"- and 0.010"-thick are symmetrically applied to either side of the core [31]. Properties consistent with those of aircraft glass were assigned to the windows of the aircraft. The beams in the model were given the material properties of aluminum. Figure B17 shows the location of the various property sections in the model.

It was assumed that the structure-borne noise produced by the engines would enter the aircraft through the wing mounting points on the fuselage. Therefore, this noise source was modeled with a total of sixteen point forces applied to the eight locations where the wings would attach to the fuselage, as shown in Figure B18. Two wing mounts are located on each side of the fuselage. Two more mounting points are located on each of the bulkheads below the baggage compartment. All the forces applied to the fuselage were steady-state, harmonic, and in-phase.

A structural damping coefficient of 3% of critical was applied to the composite structures in the problem. This value is typical for composite materials [32]. The window structures in the aircraft were given a damping value of 5% of critical in an attempt to reduce the influence of those modes on the overall acoustic solution. Though structures in the passenger cabin interior such as trim panels, seats, and passengers were not modeled directly, it was felt that some accounting should be made for the effect of these features on the acoustic behavior of the cabin. Therefore, the fluid elements in the model were assigned a damping value of 3% of critical to account for the noise attenuating effects of the aforementioned items.

4.2: Formulation of the Optimization Problem for the Starship

To reduce the acoustic pressure at a number of points inside the Starship fuselage, the objective function was minimized with the constraint that it be larger than the maximum sound pressure level for all the response points in the aircraft and for all excitation frequencies within the range of optimization.

For the optimization problem, a total of ten fluid grid points were used as acoustic pressure response locations. These points were chosen to represent the approximate listening locations of the passengers in the cabin. The acoustic pressure at each of these

points was used as a constraint in the optimization problem. The objective function was minimized at 25 frequencies equally spaced over the range of 185 Hz to 210 Hz. Thus, there were a total of 250 constraints for the optimization problem.

As was done for the cylinder sensitivity analysis in Chapter 3, the lamination angles in the fuselage composite material were used as the design variables for the problem. Unlike the cylinder, which consisted of a single-layer composite and therefore only had one lamination angle, a total of eight lamination angle design variables were available for the Starship fuselage. The lamination angles were optimized for the fuselage as one large section. As discussed above, this arrangement reflected the actual construction of the aircraft. Not included in this optimization were the windows, the passenger cabin door, and the bulkhead at the aft end of the passenger cabin.

The objective function was minimized over a range of frequencies, rather than a single frequency, in recognition of the fact that in a typical aircraft environment the structural modes can “shift” in frequency due to changes in pressure and temperature. Specification of a single optimization excitation frequency would be of limited application. Thus, to accommodate these factors, the effect of lamination angle over a range of excitation frequencies was considered.

4.3: Dynamic Analysis and Optimization of the Starship

To determine the modal truncation error in the frequency range of interest for the optimization problem, a direct frequency response was run on the same model for an excitation range of 185 to 210 Hz. The fuselage was analyzed over a wide frequency range using the modal forced frequency response method. Damping of 1% of critical was applied to the structure. No damping was applied to the fluid. A total of 500 structural and 200 fluid modes were used to model the behavior of the Starship fuselage and interior

over an excitation frequency range of 50 to 250 Hz. The 500 structural modes covered a range of excitation frequencies from 0.0 to 650.4 Hz and the 200 fluid modes covered a frequency range from 36.23 to 480.94 Hz.

A comparison of these analyses for two structural and two fluid locations in the model are shown in Figures B19, B20, B21 and B22. From these figures, there is very good agreement between the numerical direct and modal solutions over the frequency range of interest for this study. Thus, it was felt that the modal solution method could be used for the analysis and optimization of the fuselage. It was assumed that these results, which were attained for a structural damping of 1% of critical, would also be valid for the 3% damping which was applied to the fuselage for the optimization analysis.

The lamination angles in the Starship model were next optimized to reduce the interior sound pressure levels. A total of eleven design iterations were allowed for the optimization algorithm. Figure B23 shows the design cycle history for the objective function for these eleven iterations. Figure B24 displays the same information for the lamination angles in the model. Here, angles one through four represent the angles for the face sheets on the outer surface of the fuselage, while angles five through eight are the lamination angles for the graphite epoxy face sheets on the inner surface of the fuselage. The actual design variable history for the objective function from the data deck is shown below. Complete numerical data for all the design variables of the problem are shown in Table 1.

 S U M M A R Y O F D E S I G N C Y C L E H I S T O R Y

(HARD CONVERGENCE ACHIEVED)

NUMBER OF FINITE ELEMENT ANALYSES COMPLETED 12
 NUMBER OF OPTIMIZATIONS W.R.T. APPROXIMATE MODELS 11

OBJECTIVE AND MAXIMUM CONSTRAINT HISTORY

CYCLE NUMBER	OBJECTIVE FROM APPROXIMATE OPTIMIZATION	OBJECTIVE FROM EXACT ANALYSIS	FRACTIONAL ERROR OF APPROXIMATION	MAXIMUM VALUE OF CONSTRAINT
INITIAL		1.000000E+02		2.135050E-02
1	1.013803E+02	1.013803E+02	0.000000E+00	-8.522272E-03
2	1.001399E+02	1.001399E+02	0.000000E+00	5.675554E-04
3	9.959965E+01	9.959965E+01	0.000000E+00	8.283854E-04
4	9.902927E+01	9.902927E+01	0.000000E+00	3.115296E-03
5	9.873276E+01	9.873276E+01	0.000000E+00	1.069272E-02
6	9.869451E+01	9.869451E+01	0.000000E+00	5.217791E-03
7	9.844659E+01	9.844659E+01	0.000000E+00	8.577228E-03
8	9.706750E+01	9.706750E+01	0.000000E+00	2.523625E-02
9	9.831521E+01	9.831521E+01	0.000000E+00	-2.052307E-03
10	9.738248E+01	9.738248E+01	0.000000E+00	1.018381E-02
11	9.730855E+01	9.730855E+01	0.000000E+00	4.118681E-03

Cycle	Obj.	Angle 1	Angle 2	Angle 3	Angle 4	Angle 5	Angle 6	Angle 7	Angle 8
0	100.00	63.00	108.0	18.00	108.00	108.00	18.00	108.00	63.00
1	101.38	59.56	86.82	21.60	86.36	86.40	21.60	86.40	57.01
2	100.14	52.74	94.59	25.94	92.78	84.21	25.92	83.39	45.61
3	99.60	45.66	113.50	31.19	111.34	87.16	31.12	66.71	40.90
4	99.03	41.23	114.45	37.43	126.82	104.59	37.38	53.36	37.85
5	98.73	40.70	137.37	36.94	124.94	83.67	30.91	42.69	34.83
6	98.69	39.68	118.42	29.54	107.71	66.94	37.09	47.46	27.85
7	98.45	39.18	134.95	32.28	129.56	61.36	32.52	37.97	26.65
8	97.07	38.61	108.15	34.32	143.55	49.09	39.03	45.56	26.82
9	98.32	38.15	118.95	30.89	132.42	45.62	37.15	42.78	26.43
10	97.38	39.10	130.85	33.98	120.35	50.21	40.87	47.06	25.34
11	97.31	38.93	123.31	37.38	126.05	46.23	41.40	44.49	25.53

Table 1 Summary of the design cycle history of each design variable used in the optimization problem.

The data output listing provides several indicators of the validity of the optimization run. First, the fractional error of approximation is the difference between the values of the objective function calculated from the approximate model and the finite element analysis for each design cycle. A large fractional error would indicate that the move limits for the problem were too large and that smaller limits should be used. The error for each iteration of the present analysis was zero. Therefore, the move limits which were used were not too large.

The data output also indicates the maximum value of the constraints for each design cycle. From comparison to Equation (13), it would be expected that this value be negative for this optimization. However, because trying to achieve exactly zero in a computer application is not meaningful, constraints are not considered violated unless they are larger than some small positive number. Thus, not all the values listed in the data output necessarily represent violated constraints.

Not shown in the data output above, but contained in the data file, is the ending density of the design sensitivity matrix. The design sensitivity matrix is a table listing the design sensitivities for each of the responses of the problem as calculated with MSC/NASTRAN. The density indicates the percentage of nonzero terms appearing in the matrix. The ending density of this matrix for the present optimization was 91.93%. That is, 91.93% of the design responses were showing a sensitivity to changes in the design variables. A small density value would be an indicator that very few design responses were changing with changes in the design variables and that the problem may be poorly or incorrectly specified. The value for this run was quite large and indicated that nonzero sensitivities were being calculated in the optimization.

The optimization algorithm achieved hard convergence when the maximum number of design iterations allowed for the problem (eleven) was reached. The objective function

moved from a starting value of 100 dB to a final value of 97.31 dB. However, initial analysis of the cabin interior indicated that the maximum acoustic pressure in the cabin at the start of the optimization process was 101.31 dB. Thus, the initial objective function value of 100 dB was in violation of the design constraints of the problem and the value of the objective increased on the first iteration. This increase moved the objective and design variables into a usable and feasible solution region. Subsequent design cycles each reduced the value of the objective function with the exception of iteration number nine.

In Figure B24, it is apparent that the composite material is no longer symmetric after optimization. From a starting lay up of (63/108/18/108/core/108/18/108/63), the lamination angles have moved toward a lay up of (38/123/37/126/core/46/41/44/25). The four face sheets on the outer surface of the composite appear to be moving toward a cross-ply orientation (i.e. 35/125/35/125), while three of the four inner face sheets are moving to a lamination angle of 40°.

Figure B25 is a comparison of the sound pressure level before and after lamination angle optimization. Shown is the pressure over the range of optimization frequencies at the response point located near the rear window in the starboard side of the aircraft. Each peak in this region of the response corresponds to a fluid resonance. This was the response location in the passenger cabin having the largest sound pressure peak prior to optimization. A general decrease in the sound pressure levels at this location is apparent over the frequency range of optimization. In particular, the highest response peak in the region has been reduced from 101.31 dB to 97.28 dB, a reduction of 4.03 dB.

The comparison of the acoustic pressure at this same location before and after optimization is shown for a broad range of excitation frequencies in Figure B26. The limits of the optimization range are shown in this figure for reference. While the noise levels have decreased over the range of optimization frequencies, they have increased

for other frequencies in the response. In particular, a substantial increase in the acoustic pressure response is noticeable in the range from 110 Hz to 160 Hz. Comparisons of the acoustic response before and after optimization for the remaining response points in the fluid are provided in Appendix C.

The peak sound pressure level in the response occurs at an excitation frequency of 203 Hz. A fringe plot of this response before optimization is shown in Figure B27. Note that this response is very similar to a cylindrical mode shape of (1,2,3). A fringe plot of the acoustic pressure response at this same frequency after optimization is shown in Figure B28. While the shape of the response has not changes appreciably from before optimization to after, the magnitude of the response has been decreased.

Similar fringe plots are shown for the structural response at 203 Hz in Figures B29 (prior to optimization) and B30 (after optimization). From these figures, a change in the structural response is evident in the region at the bottom of the fuselage forward of the rear passenger compartment bulkhead.

To reduce the sound pressure levels in the passenger cabin, the structural modes are modified such that they no longer couple efficiently with the acoustic modes in the range of optimization frequencies. The structural modes are modified by changing the lamination angles of the fuselage sandwich composite material. The fringe plots of the structural response show that in the areas where the response has changes appreciably, it appears to be moving to a response shape which will couple less efficiently with the acoustic response shape at 203 Hz. As structural modes decouple from a particular fluid mode, they may couple with other fluid modes, thus increasing the response at those excitation frequencies. Thus, as shown in the figures for this work, the sound pressure level may actually increase at frequencies outside the range of optimization frequencies.

Recall that for this work, the optimizer did not have control over the lamination

angles in the windows of the aircraft. It was not possible to modify the response characteristics of these regions. However, the modes of the windows appeared to be significant contributors to the acoustic response in the passenger cabin. In particular, it was noted that the locations of the windows approximately coincided with the “anti-nodes” of the fluid response at 203 Hz. The contribution of these window modes coupled with the fact that contribution could not be modified with this optimization scheme may have prevented a further reduction in the passenger cabin sound pressure levels.

The acoustic pressure levels at the response points in the passenger cabin have been successfully reduced through an optimization of the lamination angles in the cabin. As anticipated, an increase in sound pressure level was noted in areas of the response outside the range of the optimization frequencies.

Chapter 5 Conclusions

The Beech Starship was modeled and the lamination angles in the fuselage were optimized to achieve a reduction in the interior noise levels. Point forces simulating the structure borne noise produced by the engines were applied to the model. These forces were the noise source for the problem. Optimization of the lamination angles was performed over a frequency range of 185 Hz to 210 Hz. Ten response locations in the fluid were used to define the constraints of the problem. The objective function was minimized with the constraint that it be equal to the maximum sound pressure level in the set of response locations. This formulation had the potential to reduce the sound pressure level at several locations and frequencies in the fuselage cabin.

Prior to optimization of the fuselage, the optimization formulation was applied to a thin, cylindrical shell. Boundary conditions and point forces were applied to the shell to facilitate the solution of the shell equations of motion by analytical means. These analytical solutions were used to validate numerical solutions for the motion of the shell and for the sensitivity of acoustic pressure to lamination angle. Particular attention was given to differences between the partially-coupled analytical solution and the fully-coupled numerical solution.

Results from the analysis of the cylinder showed good correlation between the analytical and numerical solutions. The importance of the coupling of the fluid to the motion of the cylinder became apparent in the design sensitivity analysis. The acoustic peaks in the numerical response should show some sensitivity to changes in lamination angle. The analytical solution used in this work was partially-coupled, and, as anticipated, such a sensitivity was not present in the analytical solution.

The peak acoustic response in the Starship was reduced by 4.03 dB through an optimization of the lamination angles of the structure. Similar sound pressure level reductions were attained at other locations in the passenger cabin. The optimization run was terminated after 11 iterations. The fuselage composite material was no longer symmetric after optimization. The outer four face sheets appeared to be moving toward a cross-ply configuration, while three of the four inner face sheets were moving toward the same lamination angle. Sound pressure level increased at several excitation frequencies not included in the range of frequency optimization range.

Not all areas of the fuselage structure were included in the optimization. Modes outside the portion of the structure included in the optimization were still manifested in the acoustic response after optimization and may have prevented a further reduction in noise level.

This work has successfully demonstrated the feasibility of reducing aircraft interior noise over a range of excitation frequencies through optimization of the composite lamination angles of the aircraft. Significantly, this noise reduction was attained on an actual aircraft model, rather than a thin, cylindrical shell fuselage model. A reduction in sound pressure level was also achieved at a number of points in the cabin interior and over a range of excitation frequencies.

Careful consideration must be given to which areas of the aircraft are to be optimized and over what frequency range the optimization should take place. Areas of the fuselage which are not included in the lamination angle optimization may still have an effect upon the acoustic response after optimization. For frequencies not included in the optimization range, the acoustic pressure can increase after optimization. Care must be exercised to ensure that an acoustic response field is not created that passengers would find more unpleasant than the original acoustic field.

This work did not consider any effects that lamination angle optimization might have upon the structural integrity of the aircraft. Clearly, these effects cannot be ignored by the aircraft manufacturer and they would take precedence over the acoustic benefits of this analysis.

This work used point sources to model the structure-borne noise produced by the engines. As an extension of this work, the model could be modified to include other noise sources. Some of these sources might be propeller noise or boundary layer noise. The effects of changing the mounting locations of the engine could also be investigated. For example, many small airplanes the same size class as the Starship have engines mounted on the aft portion of the fuselage, rather than on the wings. Investigations of these types would be of great applicability to the aircraft manufacturing industry.

Chapter 6 Acknowledgments

The first author gratefully acknowledges support from NASA Langley Research Center and The George Washington University throughout the course of this work.

Bibliography

- [1] Hashin, Zi, ed. *Mechanics of Composite Materials: Recent Advances*. Proceedings of the IUTAM Symposium on Mechanics of Composite Materials, Pergamon Press, 1982.
- [2] Jones, Robert M. *Mechanics of Composite Materials*. Scripta Book Company, Washington, D. C., 1975.
- [3] Koval, L. R. "Sound Transmission into a Laminated Composite Cylindrical Shell." *Journal of Sound and Vibration*, Vol. 71, No. 4, 1980.
- [4] Silcox, Richard J., Lester, Harold C., and Abler, Steve B. "An Evaluation of Active Noise Control in a Cylindrical Shell." NASA TM 89090, February 1987.
- [5] Salagame, R. R., Belegundu, A. D., and G. H. Koopmann. "Analytical Sensitivity of Acoustic Power Radiated from Plates." *Journal of Vibration and Acoustics*, Vol. 117, January 1995.
- [6] Lamancusa, J. S. "Numerical Optimization Techniques for Structural-Acoustic Design of Rectangular Panels." *Computers and Structures*, Vol. 48, No. 4, 1993.
- [7] Naghshineh, Koorosh, Koopmann, Gary H., and Belegundu, Ashok D. "Material Tailoring of Structures to Achieve a Minimum Radiation Condition." *Journal of the Acoustical Society of America*, 92(2), Pt. 1, August 1992.
- [8] Engelstad, S. P., Cunefare, K. A., Crane, S., and Powell, E. A. "Optimization Strategies for Minimum Interior Noise and Weight Using FEM/BEM." *Inter-Noise 95 Proceedings*, 1995.
- [9] Crane, S. P., Cunefare, K. A., Engelstad, S. P. and Powell, E. A. "A Comparison of Optimization Formulations for Design Minimization of Aircraft Interior Noise." *37th AIAA Structural Dynamics and Mechanics Conference*, AIAA 96-1480, April 1996.

- [10] Rao, K. P. and Gopalkrishna, H. R. "Optimization of Composite Cylindrical Panels for Buckling by Ranking." *Composite Structures*, Vol. 21, No. 3, 1992.
- [11] Hu, Hsuan-Teh and Wang, Su Su. "Optimization for Buckling Resistance of Fiber-Composite Laminate Shells with and without Cutouts." *Composite Structures*, Vol. 22, No. 1, 1992.
- [12] MacNeal, Richard H. *NASTRAN Theoretical Manual*. The MacNeal-Schwendler Corporation, 1972.
- [13] Marulo, Francesco and Beyer, Todd B. "NASTRAN Application for the Prediction of Aircraft Interior Noise." *Fifteenth NASTRAN Users' Colloquium*, NASA CP 2481, May 1987.
- [14] Grosveld, Ferdinand W., Sullivan, Brenda M., and Marulo, Francesco. "Aircraft Interior Noise Prediction Using a Structural-Acoustic Analogy in NASTRAN Modal Synthesis." *Proceedings of the 6th International Modal Analysis Conference*, Kissimmee, Florida, Volume 2, 1988.
- [15] SenGupta, G., Landmann, A. E., Mera, A., and Yantis, T. F. "Prediction of Structure-Borne Noise, Based on the Finite Element Method." *AIAA 10th Aeroacoustics Conference*, AIAA-86-1861, July 1986.
- [16] Fernholz, Christian M. and Robinson, Jay H. "Fully-Coupled Fluid/Structure Vibration Analysis Using MSC/NASTRAN." NASA TM 110215, January 1996.
- [17] Reddy, J. N. *An Introduction to the Finite Element Method*. McGraw-Hill, 2nd ed., 1993.
- [18] Lahey, Robert S., *et al.*, editors. *MSC/NASTRAN Reference Manual, Version 68, Volume 1*. The MacNeal-Schwendler Corporation, 1994.
- [19] Blakely, Ken. *MSC/NASTRAN Basic Dynamic Analysis, Version 68*. The MacNeal-Schwendler Corporation, 1993.

- [20] Roozen, N. B. “Numerical Acousto-elastic Analysis of Aircraft Structures using MSC/NASTRAN”. *1993 MSC European User’s Conference*, 1993.
- [21] *Fluid-Structure Analysis in MSC/NASTRAN*. Seminar notes. The MacNeal Schwendler Corporation, 1993.
- [22] Moore, Gregory J. *MSC/NASTRAN Design Sensitivity and Optimization, Version 68*. The MacNeal-Schwendler Corporation, 1994.
- [23] Vanderplaats, Garret N. “CONMIN-A FORTRAN Program for Constrained Function Minimization User’s Manual.” NASA TM X-62,282, August 1973.
- [24] *Design Sensitivity and Optimization in MSC/NASTRAN*. Seminar notes. The MacNeal Schwendler Corporation, 1995.
- [25] Unruh, J. F. and Dobosz, S. A. “Fuselage Structural-Acoustic Modeling for Structure-Borne Interior Noise Transmission.” *Journal of Vibration, Acoustics, Stress, and Reliability in Design*, Vol. 110, April 1988.
- [26] Bert, C. W. *et al.* “Free Vibrations of Multilayer Anisotropic Cylindrical Shells.” *Journal of Composite Materials*, Vol. 3, July 1969.
- [27] Hu, Hsuan-Teh and Wang, Su Su. “Optimization for Buckling Resistance of Fiber-Composite Laminate Shells with and without Cutouts.” *Composite Structures*, Vol. 22, No. 1, 1992.
- [28] Dong, Stanley B. “Free Vibration of Laminated Orthotropic Cylindrical Shells.” *The Journal of the Acoustical Society of America*, Vol. 44, No. 6, 1968.
- [29] Leissa, Arthur W. *Vibration of Shells*. USGPO, NASA SP-288, 1973.
- [30] Hooper, E. H. “Structural Development of Recent Aircraft — Starship.” *36th AIAA/ASME/ASCE/AHS/ASC Structures, Structural Dynamics and materials Conference*, AIAA 95-1469, April 1995.

- [31] Hooper, E. H. "Starship: A Model for Future Designs." *The First Core Conference*, Zurich, October 1988.
- [32] Coates, Timothy J. "A Numerical Study of Active Structural Acoustic Control in a Double Wall Cylinder." Master's thesis, The George Washington University, August 1993.
- [33] Lester, Harold C. and Lefebvre, Sylvie. "Piezoelectric Actuator Models for Active Sound and Vibration Control of Cylinders." *Journal of Intelligent Material Systems and Structures*, July 1993.
- [34] Kraus, Harry. *Thin Elastic Shells*. John Wiley & Sons, Inc., 1967.
- [35] Press, William H. *Numerical Recipes: The Art of Scientific Computing*. Cambridge University Press, first edition, 1990.
- [36] Wolfram, Stephen. *MathematicaTM: A System for doing Mathematics by Computer*. Addison-Wesley Publishing Company, Inc., 1988.
- [37] Reymond, Michael and Miller, Mark, Editors. *MSC/NASTRAN Quick Reference Guide, Version 68*. The MacNeal-Schwendler Corporation.

Appendix A Equations of Motion for a Thin, Specially Orthotropic Cylindrical Shell

In this appendix, a solution for the thin cylindrical shell equations of motion for specially orthotropic materials is developed. The Donnell-Mushtari equations of motion are summarized. More detailed theories are available. For these theories, the reader is referred to the literature [29, 34]. A solution for a particular set of boundary conditions and applied forces is given. This solution was in turn used for work appearing in Chapter 3 of this research. A solution is also developed for the fluid inside the shell.

The Donnell-Mushtari equations of motion for a thin, specially orthotropic single-layer circular cylinder including damping effects are given by [29, 33]:

$$\begin{bmatrix} L_{11} & L_{12} & L_{13} \\ L_{21} & L_{22} & L_{23} \\ L_{31} & L_{32} & L_{33} \end{bmatrix} \begin{bmatrix} u \\ v \\ w \end{bmatrix} = \frac{(1 - \nu_{\theta x} \nu_{x\theta})}{E_{xx} h} \begin{bmatrix} f_x \\ f_\theta \\ f_r \end{bmatrix} \quad (\text{A1})$$

where

$$\begin{aligned} L_{11} &= \frac{\partial^2}{\partial s^2} + \frac{G(1 - \nu_{\theta x} \nu_{x\theta})}{E_{xx}} \frac{\partial^2}{\partial \theta^2} + \gamma \frac{(1 - \nu_{\theta x} \nu_{x\theta})}{E_{xx} h} \frac{\partial}{\partial t} - \frac{\rho_s a^2 (1 - \nu_{\theta x} \nu_{x\theta})}{E_{xx}} \frac{\partial^2}{\partial t^2} \\ L_{12} &= \frac{\nu_{x\theta} E_{\theta\theta} + G(1 - \nu_{\theta x} \nu_{x\theta})}{E_{xx}} \frac{\partial^2}{\partial s \partial \theta} \\ L_{13} &= \frac{\nu_{\theta x} E_{\theta\theta}}{E_{xx}} \frac{\partial}{\partial s} \\ L_{21} &= \frac{\nu_{x\theta} E_{\theta\theta} + G(1 - \nu_{\theta x} \nu_{x\theta})}{E_{xx}} \frac{\partial^2}{\partial s \partial \theta} \\ L_{22} &= \frac{G(1 - \nu_{\theta x} \nu_{x\theta})}{E_{xx}} \frac{\partial^2}{\partial s^2} + \frac{E_{\theta\theta}}{E_{xx}} \frac{\partial^2}{\partial \theta^2} + \gamma \frac{(1 - \nu_{\theta x} \nu_{x\theta})}{E_{xx} h} \frac{\partial}{\partial t} - \frac{\rho_s a^2 (1 - \nu_{\theta x} \nu_{x\theta})}{E_{xx}} \frac{\partial^2}{\partial t^2} \\ L_{23} &= \frac{E_{\theta\theta}}{E_{xx}} \frac{\partial}{\partial \theta} \\ L_{31} &= \frac{\nu_{x\theta} E_{\theta\theta}}{E_{xx}} \frac{\partial}{\partial s} \\ L_{32} &= \frac{E_{\theta\theta}}{E_{xx}} \frac{\partial}{\partial \theta} \\ L_{33} &= \frac{E_{\theta\theta}}{E_{xx}} + \frac{h^2}{12a^2} \left[\frac{\partial^4}{\partial s^4} + 2 \frac{\nu_{x\theta} E_{\theta\theta} + 2G(1 - \nu_{\theta x} \nu_{x\theta})}{E_{xx}} \frac{\partial^4}{\partial s^2 \partial \theta^2} + \frac{E_{\theta\theta}}{E_{xx}} \frac{\partial^4}{\partial \theta^4} \right] \\ &\quad + \gamma \frac{(1 - \nu_{\theta x} \nu_{x\theta})}{E_{xx} h} \frac{\partial}{\partial t} + \frac{\rho_s a^2 (1 - \nu_{\theta x} \nu_{x\theta})}{E_{xx}} \frac{\partial^2}{\partial t^2} \end{aligned} \quad (\text{A2})$$

where

$$s = \frac{x}{a} \quad (\text{A3})$$

Here, u , v , and w represent the axial, circumferential, and radial displacements of the middle surface of the shell, h represents the shell thickness, a its radius and γ is the structural damping coefficient. On the right-hand side, f_x , f_θ , f_r represent forces applied to the cylinder in the longitudinal, circumferential, and radial directions respectively. If boundary conditions of

$$\begin{aligned} v(\theta, 0) &= v(\theta, l) = 0 \\ w(\theta, 0) &= w(\theta, l) = 0 \end{aligned} \quad (\text{A4})$$

$$u, v, w(\theta, x) = u, v, w(\theta + 2n\pi, x) \quad (\text{periodicity})$$

are applied and one assumes a harmonic time dependance, then a general solution for Equation (A1) can be written

$$\begin{aligned} u(\theta, x, t) &= e^{i\omega t} \sum_{m=0}^{\infty} \sum_{n=0}^{\infty} \cos(\lambda_m s) [U_{mn} \cos(n\theta) + U_{mn}^* \sin(n\theta)] \\ v(\theta, x, t) &= e^{i\omega t} \sum_{m=1}^{\infty} \sum_{n=0}^{\infty} \sin(\lambda_m s) [V_{mn} \sin(n\theta) + V_{mn}^* \cos(n\theta)] \\ w(\theta, x, t) &= e^{i\omega t} \sum_{m=1}^{\infty} \sum_{n=0}^{\infty} \sin(\lambda_m s) [W_{mn} \cos(n\theta) + W_{mn}^* \sin(n\theta)] \end{aligned} \quad (\text{A5})$$

where

$$\lambda_m = \frac{m\pi a}{l} \quad (\text{A6})$$

The boundary conditions shown in Equation (A4) are commonly referred to as the boundary conditions for a “shear diaphragm”, or “free support” [29]. It should be stressed that this particular set of boundary conditions was applied so as to make it possible to write a closed-form solution for Equation (A1). Proceeding with this derivation, if point

forces of

$$\begin{aligned}
 f_x &= 0 \\
 f_\theta &= 0 \\
 f_r &= F_o e^{i\omega t} \delta\left(x - \frac{l}{2}\right) [\delta(\theta) + \delta(\theta - \pi)]
 \end{aligned} \tag{A7}$$

are applied to the cylinder, the radial force can be expanded in terms of the eigen functions of the cylinder's radial displacement

$$f_r(\theta, x, t) = e^{i\omega t} \sum_{m=1}^{\infty} \sum_{n=1}^{\infty} \sin(\lambda_m s) [F_{mn} \cos(n\theta) + F_{mn}^* \sin(n\theta)] \tag{A8}$$

where

$$\begin{aligned}
 F_{mn} &= F_o \frac{2a}{\pi l} \sin\left(\frac{m\pi}{2}\right) [\cos(n\pi) + 1] \\
 F_{mn}^* &= 0
 \end{aligned} \tag{A9}$$

Note that F_{mn}^* becomes zero for this particular choice of \vec{f} . Substituting Equations (A5) and (A8) into Equation (A1) yields, after some rearrangement

$$\begin{bmatrix} a_{11} + \Omega & a_{12} & a_{13} \\ a_{21} & a_{22} + \Omega & a_{23} \\ a_{31} & a_{32} & a_{33} - \Omega \end{bmatrix} \begin{bmatrix} U_{mn} \\ V_{mn} \\ W_{mn} \end{bmatrix} = \frac{1}{\rho_s h a^2} \begin{bmatrix} 0 \\ 0 \\ F_{mn} \end{bmatrix} \tag{A10}$$

and

$$\begin{bmatrix} a_{11} + \Omega & -a_{12} & a_{13} \\ -a_{21} & a_{22} + \Omega & -a_{23} \\ a_{31} & -a_{32} & a_{33} - \Omega \end{bmatrix} \begin{bmatrix} U_{mn}^* \\ V_{mn}^* \\ W_{mn}^* \end{bmatrix} = \frac{1}{\rho_s h a^2} \begin{bmatrix} 0 \\ 0 \\ F_{mn}^* \end{bmatrix} = \vec{0} \tag{A11}$$

where

$$\begin{aligned}
a_{11} &= 2\eta i\omega\omega_{mn} - \frac{C_L^2}{a^2} \left\{ \lambda_m^2 + n^2 \frac{G(1 - \nu_{\theta x}\nu_{x\theta})}{E_{xx}} \right\} \\
a_{12} &= \frac{C_L^2}{a^2} n\lambda_m \frac{\nu_{\theta x}E_{\theta\theta} + G(1 - \nu_{\theta x}\nu_{x\theta})}{E_{xx}} \\
a_{13} &= \frac{C_L^2}{a^2} \lambda_m \frac{\nu_{\theta x}E_{\theta\theta}}{E_{xx}} \\
a_{21} &= \frac{C_L^2}{a^2} n\lambda_m \frac{\nu_{\theta x}E_{\theta\theta} + G(1 - \nu_{\theta x}\nu_{x\theta})}{E_{xx}} \\
a_{22} &= 2\eta i\omega\omega_{mn} - \frac{C_L^2}{a^2} \left\{ \lambda_m^2 \frac{G(1 - \nu_{\theta x}\nu_{x\theta})}{E_{xx}} + n^2 \frac{E_{\theta\theta}}{E_{xx}} \right\} \\
a_{23} &= -\frac{C_L^2}{a^2} n \frac{\nu_{\theta x}E_{\theta\theta}}{E_{xx}} \\
a_{31} &= -\frac{C_L^2}{a^2} \lambda_m \frac{\nu_{\theta x}E_{\theta\theta}}{E_{xx}} \\
a_{32} &= \frac{C_L^2}{a^2} n \frac{\nu_{\theta x}E_{\theta\theta}}{E_{xx}} \\
a_{33} &= 2\eta i\omega\omega_{mn} + \frac{C_L^2}{a^2} \frac{h^2}{12a^2} \left\{ \lambda_m^4 + 2n^2\lambda_m^2 \frac{\nu_{\theta x}E_{\theta\theta} + 2G(1 - \nu_{\theta x}\nu_{x\theta})}{E_{xx}} + n^4 \frac{E_{\theta\theta}}{E_{xx}} \right\}
\end{aligned} \tag{A12}$$

and

$$\begin{aligned}
C_L^2 &= \frac{E_{xx}}{\rho_s(1 - \nu_{\theta x}\nu_{x\theta})} \\
\Omega &= \frac{\rho_s a^2 (1 - \nu_{\theta x}\nu_{x\theta})}{E_{xx}} \omega^2 = \frac{a^2}{C_L^2} \omega^2
\end{aligned} \tag{A13}$$

Note that the structural damping coefficient γ has been replaced by a frequency-dependent modal damping term η where

$$\frac{\gamma}{a^2 \rho_s h} = 2\eta\omega_{mn} \tag{A14}$$

It can be seen from examination of Equations (A10) and (A11) that it is not necessary to carry along both sets of terms. Either the starred or unstarred terms can be used as a complete solution. For the case of eigenvalue analysis, both Equations (A10) and (A11) will yield the same eigenvalues. Furthermore, for the forced frequency response analysis where the applied forces are as shown in Equation (A7), the right-hand side of Equation (A11) becomes zero. Thus, the starred coefficients are also zero. This work uses the

unstarred terms of Equation (A5) as a complete solution. That is

$$\begin{aligned}
u(\theta, x, t) &= e^{i\omega t} \sum_{m=0}^{\infty} \sum_{n=0}^{\infty} U_{mn} \cos(\lambda_m s) \cos(n\theta) \\
v(\theta, x, t) &= e^{i\omega t} \sum_{m=1}^{\infty} \sum_{n=0}^{\infty} V_{mn} \sin(\lambda_m s) \sin(n\theta) \\
w(\theta, x, t) &= e^{i\omega t} \sum_{m=1}^{\infty} \sum_{n=0}^{\infty} W_{mn} \sin(\lambda_m s) \cos(n\theta)
\end{aligned} \tag{A15}$$

For the fluid-filled region inside the cylindrical shell, the wave equation in cylindrical coordinates can be used to describe the acoustic pressure at any point in the fluid. The wave equation is given by

$$\nabla^2 p - \frac{1}{c_o^2} \frac{\partial^2 p}{\partial t^2} = 0 \tag{A16}$$

where, in cylindrical coordinates,

$$\nabla^2 = \frac{\partial^2}{\partial r^2} + \frac{1}{r} \frac{\partial}{\partial r} + \frac{1}{r^2} \frac{\partial^2}{\partial \theta^2} + \frac{\partial^2}{\partial x^2} \tag{A17}$$

Choosing boundary conditions of

$$\begin{aligned}
p(r, \theta, 0, t) &= p(r, \theta, l, t) = 0 \\
\frac{\partial p(a, \theta, x, t)}{\partial r} &= -\rho_f \frac{\partial^2 w(\theta, x, t)}{\partial t^2} \\
|p(0, \theta, x, t)| &< \infty \text{ (boundedness)}
\end{aligned} \tag{A18}$$

$$p(r, \theta, x, t) = p(r, \theta + 2\pi n, x, t) \text{ (periodicity)}$$

allows one to couple the motion of the fluid to that of the cylinder and still write a relatively simple closed-form solution for the acoustic pressure in the fluid. It should be noted that this particular set of boundary conditions is chosen so that a simple closed-form solution can be developed for validation and comparison to numerical finite element solutions. This same method was used by SenGupta *et al.* [15] for the same purpose. Applying these boundary conditions and using the results for the cylindrical shell yields the following expression for p

$$p(r, \theta, x, t) = e^{i\omega t} \sum_{m=1}^{\infty} \sum_{n=1}^{\infty} J_n(\alpha_m r) \sin(\lambda_m s) [P_{mn} \cos(n\theta) + P_{mn}^* \sin(n\theta)] \tag{A19}$$

where J_n represents the n -th order Bessel function of the first kind and, written in closed-form,

$$P_{mn} = \frac{C_{mn}\rho_f\omega^2}{\frac{n}{a}J_n(\alpha_m a) - \alpha_m J_{n+1}(\alpha_m a)} \quad (\text{A20})$$

$$P_{mn}^* = 0$$

and

$$\alpha_m^2 = \frac{\omega^2}{c_o^2} - \frac{m^2\pi^2}{l^2} \quad (\text{A21})$$

As was the case for the structure, note that for the forces applied to the cylinder as shown in Equation (A7), the starred terms in Equation (A19) become zero. This work will take

$$p(r, \theta, x, t) = e^{i\omega t} \sum_{m=1}^{\infty} \sum_{n=1}^{\infty} P_{mn} J_n(\alpha_m r) \sin(\lambda_m s) \cos(n\theta) \quad (\text{A22})$$

Appendix B Figures

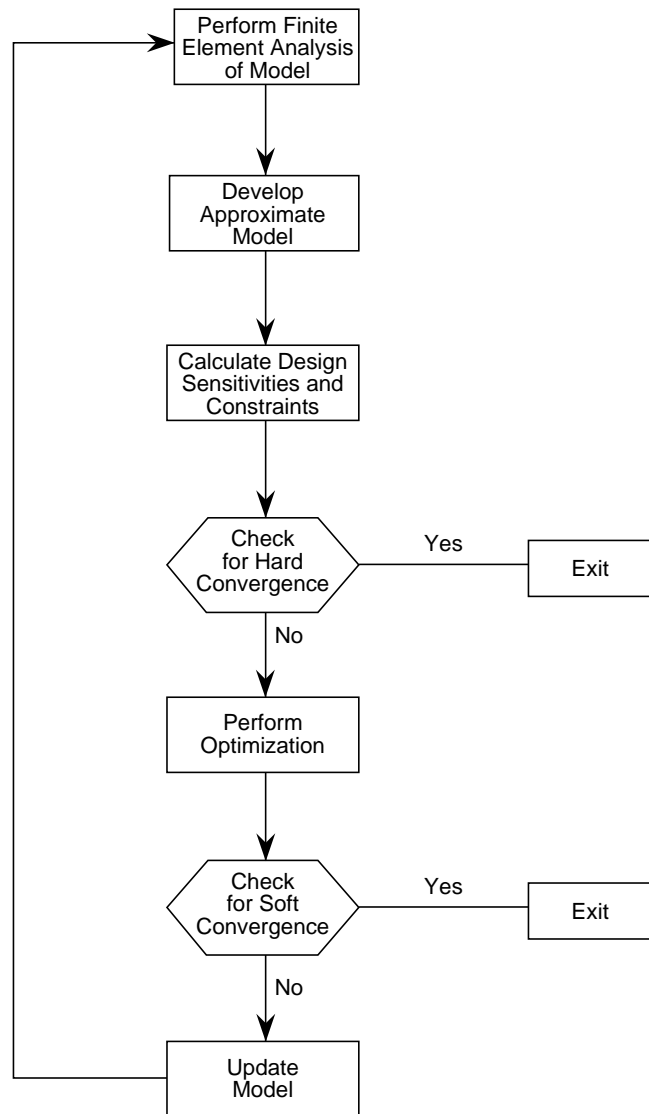


Figure B1 MSC/NASTRAN design cycle flow chart [24].

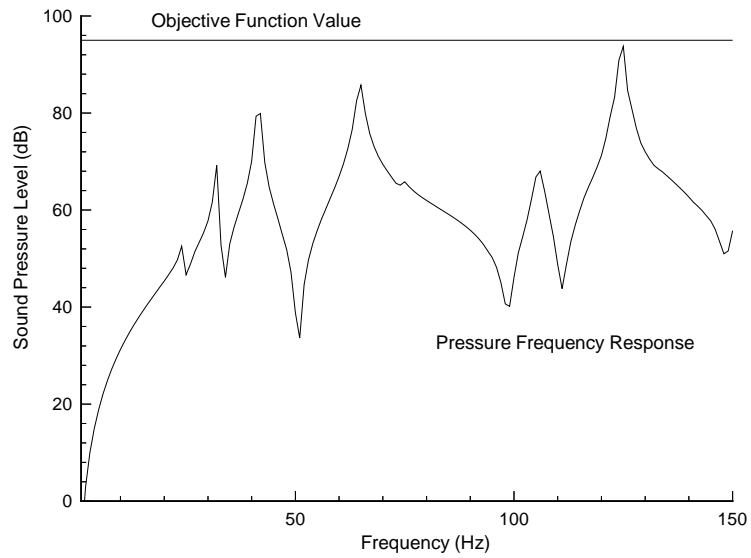


Figure B2 Schematic representation of objective function and acoustic response. As the objective function is minimized, the sound pressure level is likewise reduced.

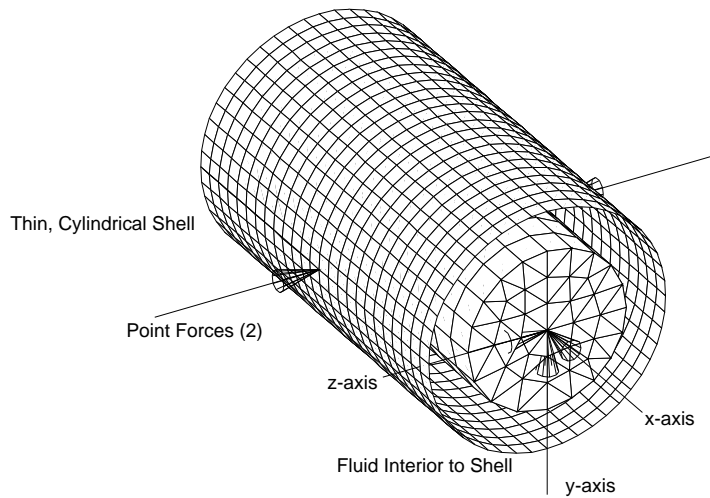


Figure B3 Exploded view of the fluid-structure problem for the thin, cylindrical shell filled with air. The forces applied to the model for this analysis are also shown.

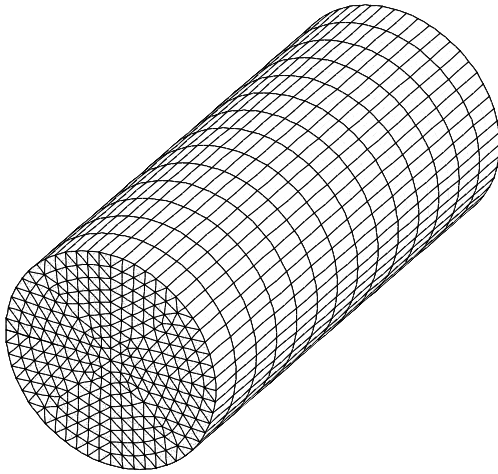


Figure B4 Finite element fluid-structure model for the thin, cylindrical shell filled with air.

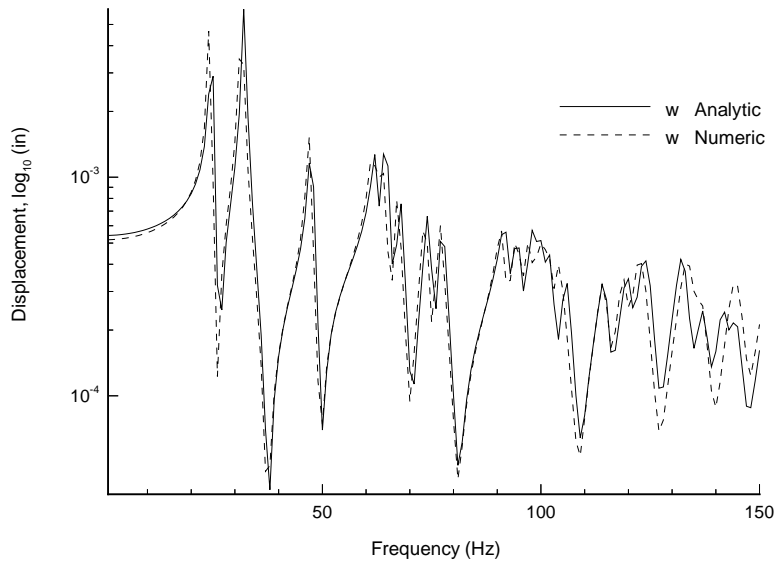


Figure B5 Radial displacement of a thin, cylindrical shell over a range of excitation frequencies. Displacement is calculated at the point $r = a$, $\theta = 0$, $x = \frac{l}{2}$. Analytical and numerical modal solutions shown.

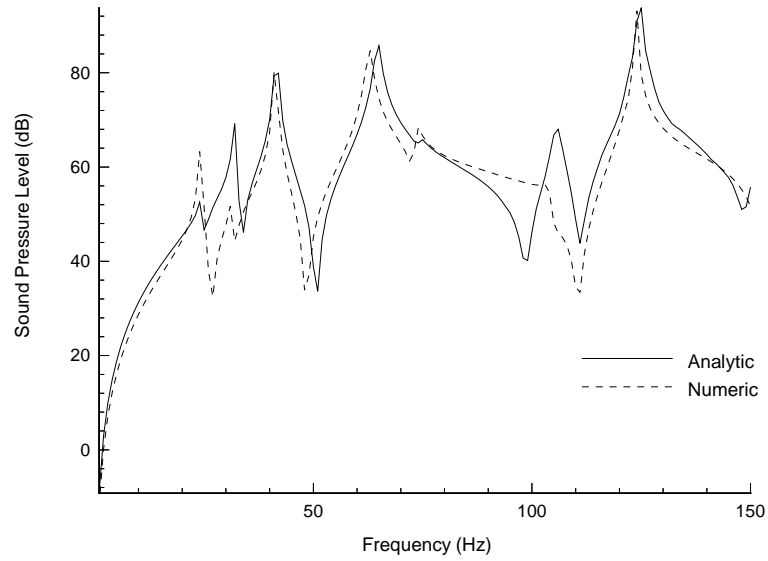


Figure B6 Sound pressure level within the thin, cylindrical shell over a range of excitation frequencies. Pressure is calculated at the fluid point at $r = \frac{a}{2}$, $\theta = 0$, $x = \frac{l}{2}$. Analytical and numerical modal solutions shown.

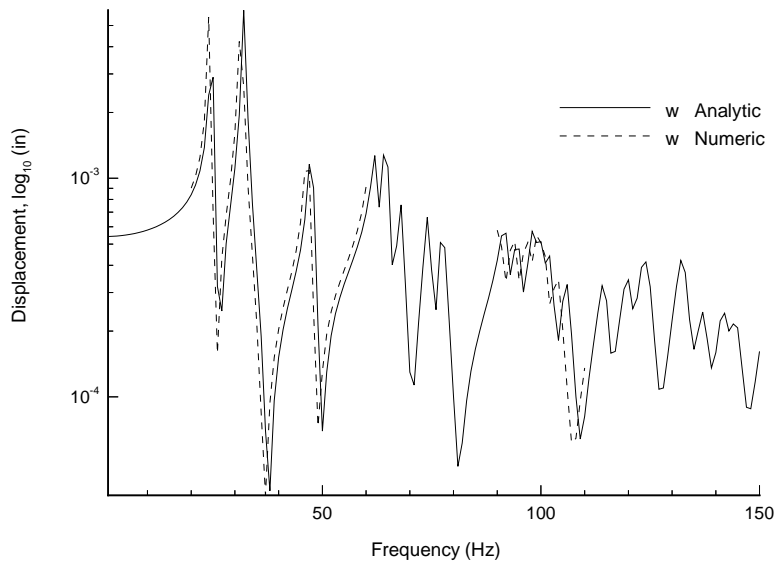


Figure B7 Radial displacement of a thin, cylindrical shell over a range of excitation frequencies. Displacement is calculated at the point $r = a$, $\theta = 0$, $x = \frac{l}{2}$. Analytical and numerical direct solutions shown. The numerical solution is for the ranges of 20 to 60 Hz and 90 to 110 Hz.

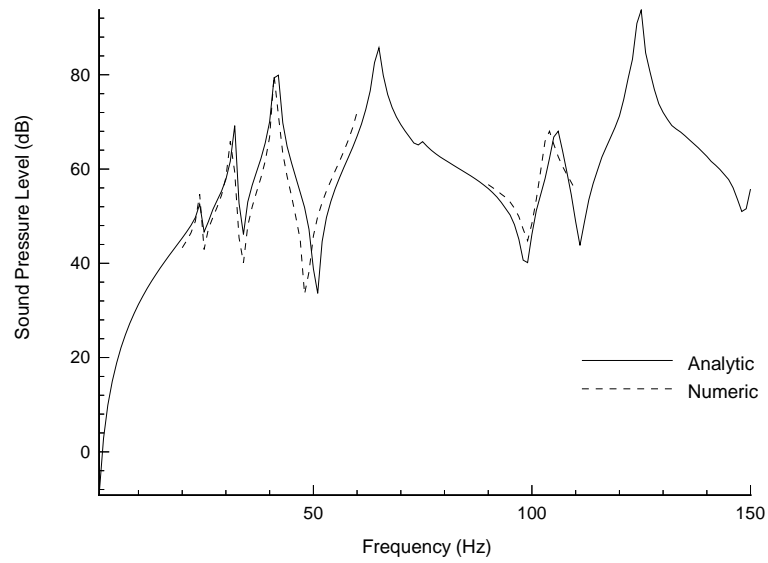


Figure B8 Sound pressure level in a thin, cylindrical shell over a range of excitation frequencies. Displacement is calculated at the point $r = \frac{a}{2}$, $\theta = 0$, $x = \frac{l}{2}$. Analytical and numerical direct solutions shown. The numerical solution is for the ranges of 20 to 60 Hz and 90 to 110 Hz.

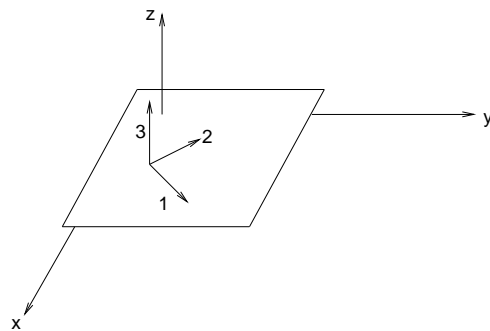


Figure B9 Global and local material axes for a single-ply laminate. The lamination angle ψ is measured counter clockwise from the global x-axis to the local material 1-axis [27].

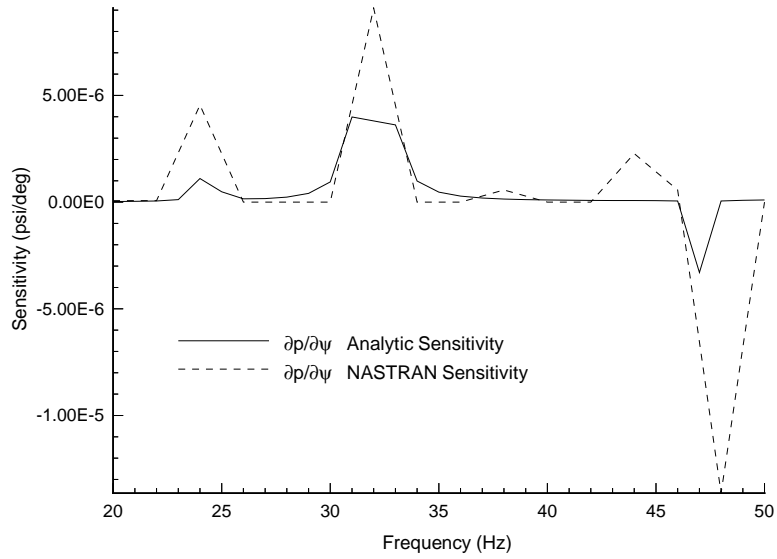


Figure B10 Sensitivity of acoustic pressure in the orthotropic cylinder with respect to changes in lamination angle ψ . Data for $\psi=0^\circ$ at fluid location $r = 0.88a$, $\theta = 75.61^\circ$, $x = 0.21l$.

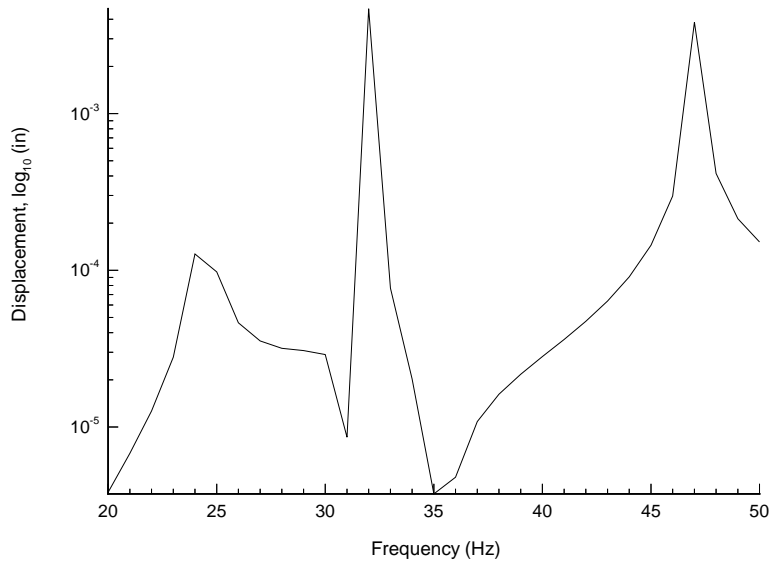


Figure B11 Analytical radial displacement at structural location $\theta = 75.61^\circ$, $x = 0.21l$.

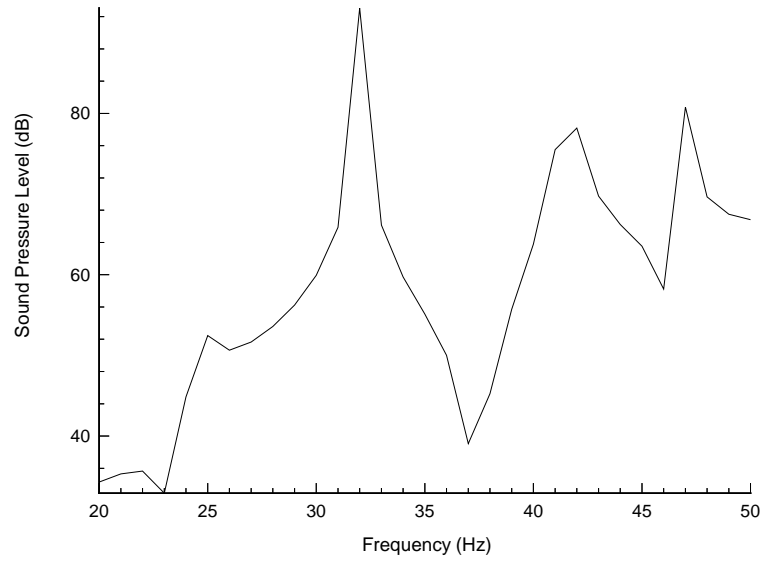


Figure B12 Analytical acoustic response at fluid location $r = 0.88a$, $\theta = 75.61^\circ$, $x = 0.21l$.

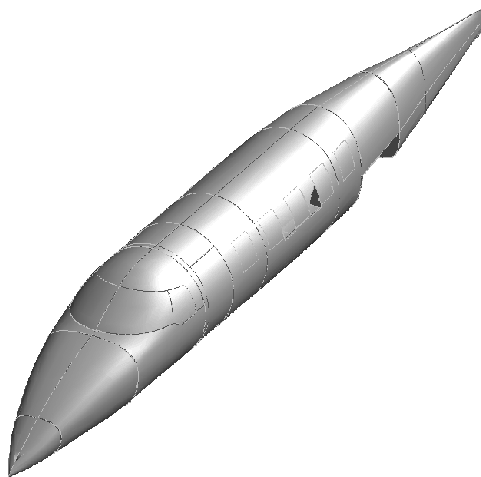


Figure B13 Isometric view of the Starship fuselage.

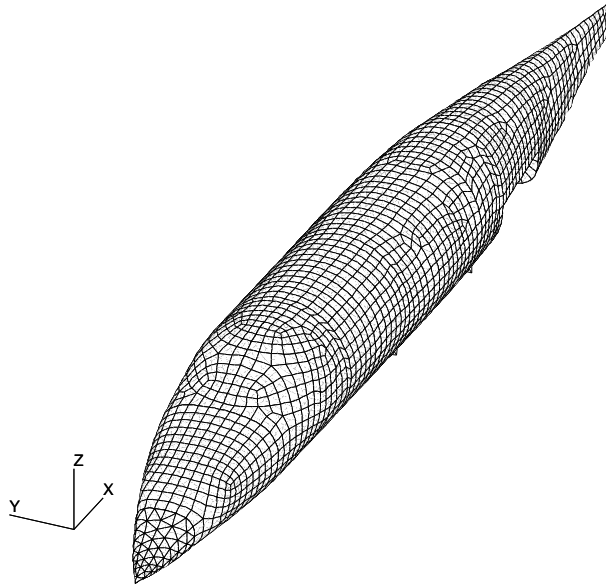


Figure B14 Isometric view of the finite element mesh of the Starship fuselage. The fluid portion of the model is not visible, as it is completely enclosed by the structural elements of the model.

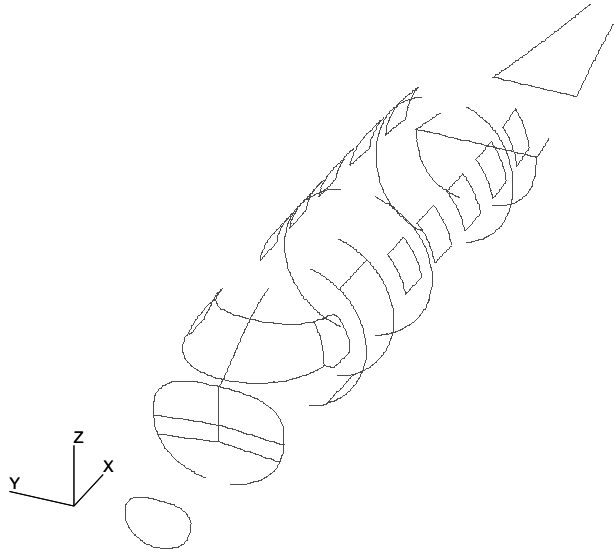


Figure B15 Isometric view of the beam elements in the Starship finite element model.

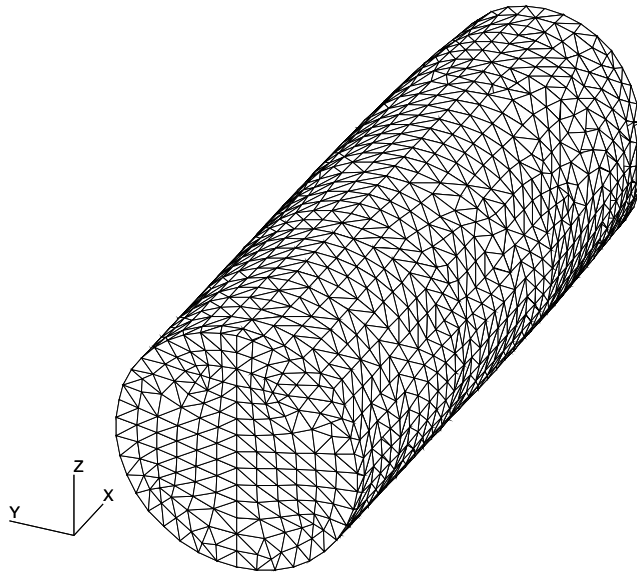


Figure B16 Isometric view of the finite element mesh of the fluid inside the Starship cabin. In the complete model of the Starship, these elements are completely enclosed by structural elements.

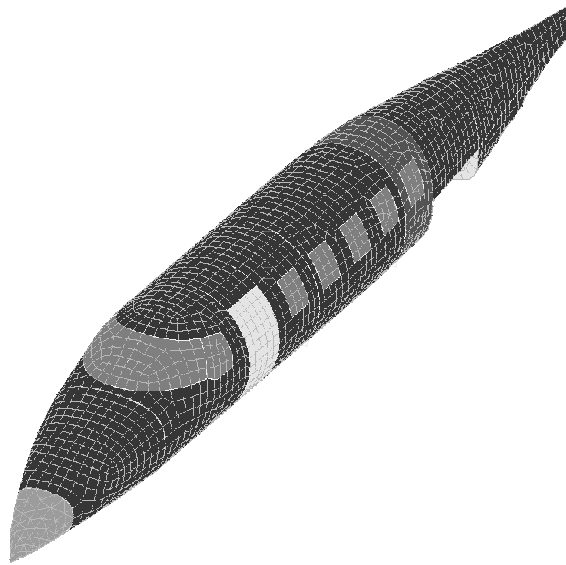


Figure B17 Isometric view of the Starship structure showing the location of the different materials used in the model.

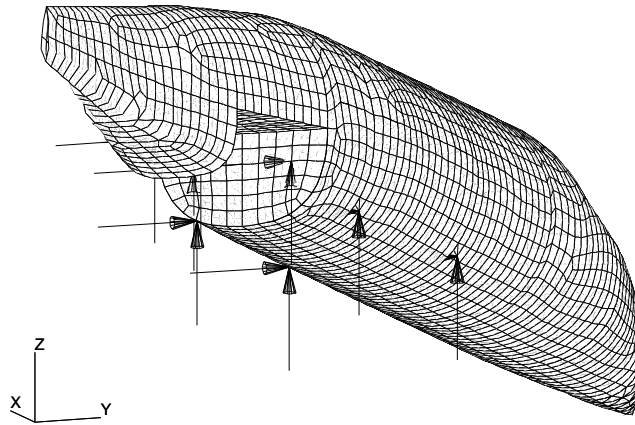


Figure B18 View of the Starship fuselage showing forces applied for this study. Shown are the forces on the wing mounts and the forward bulkhead below the baggage compartment.

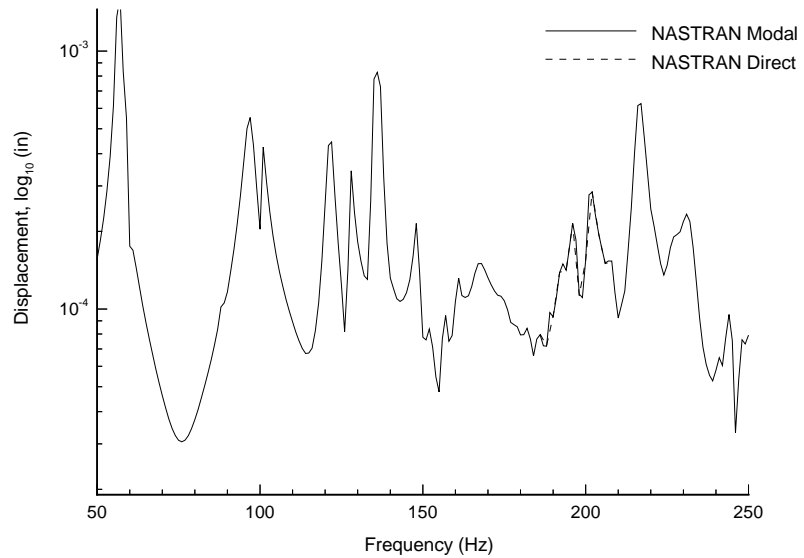


Figure B19 Forced frequency response for the Starship finite element model. Structural displacement magnitude at the point $x=253.63$, $y=-34.71$, $z=99.93$ (see Appendix C for an explanation of the Starship coordinate system).

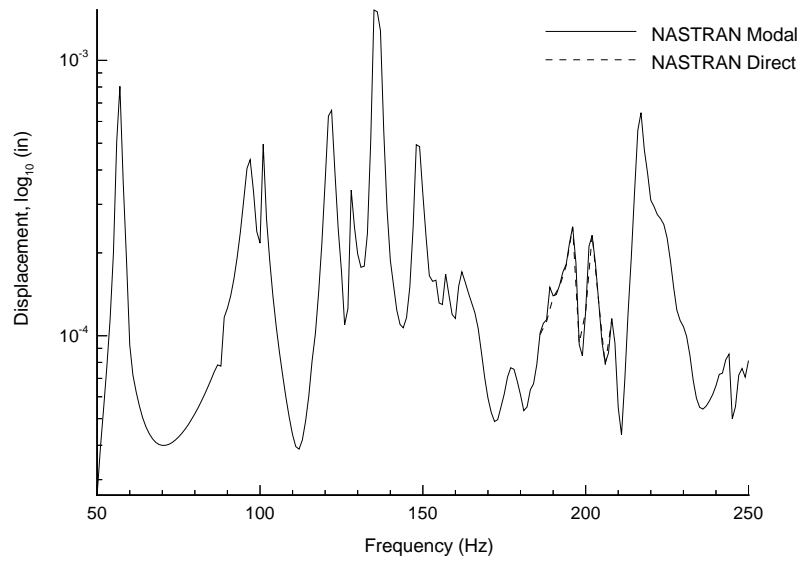


Figure B20 Forced frequency response for the Starship finite element model. Structural displacement magnitude at the point $x=293.09$, $y=-22.57$, $z=131.7$.

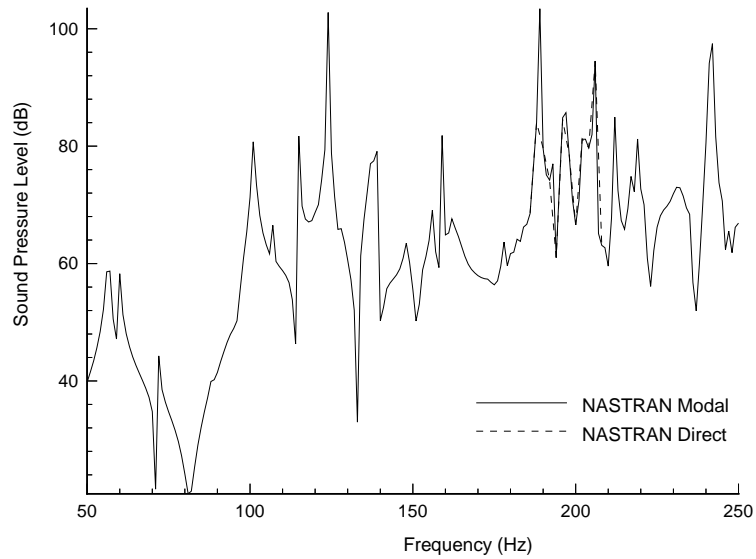


Figure B21 Forced frequency response for the Starship finite element model. Acoustic sound pressure level at the point $x=189.44$, $y=30.10$, $z=105.43$.

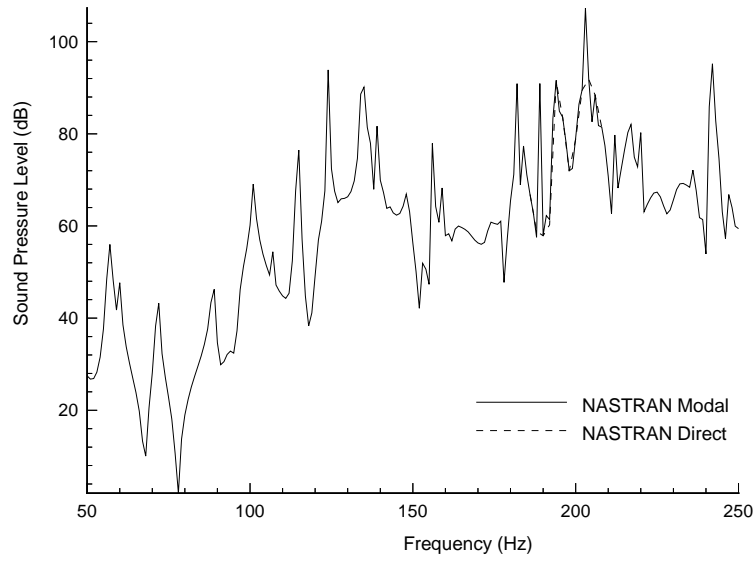


Figure B22 Forced frequency response for the Starship finite element model. Acoustic sound pressure level at the point $x=259.05$, $y=-18.52$, $z=129.15$.

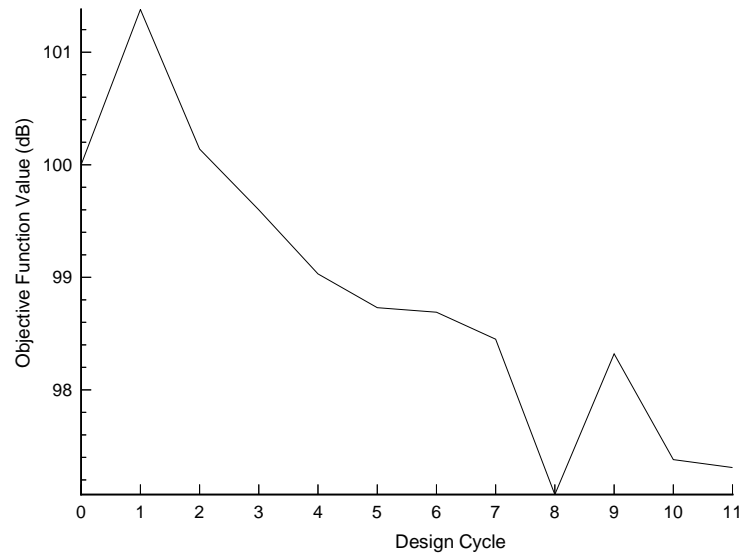


Figure B23 Design cycle history for the objective function used in the optimization problem.

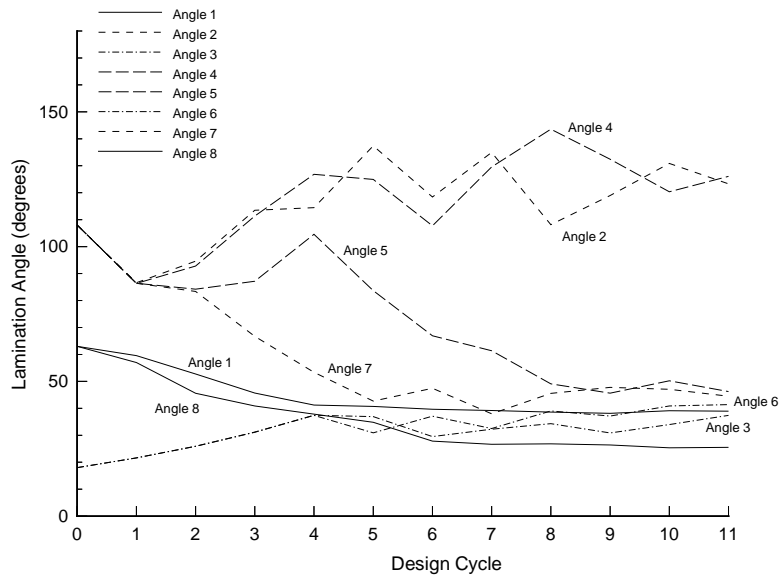


Figure B24 Design cycle history for the design variables (i.e. the lamination angles) used in the optimization problem

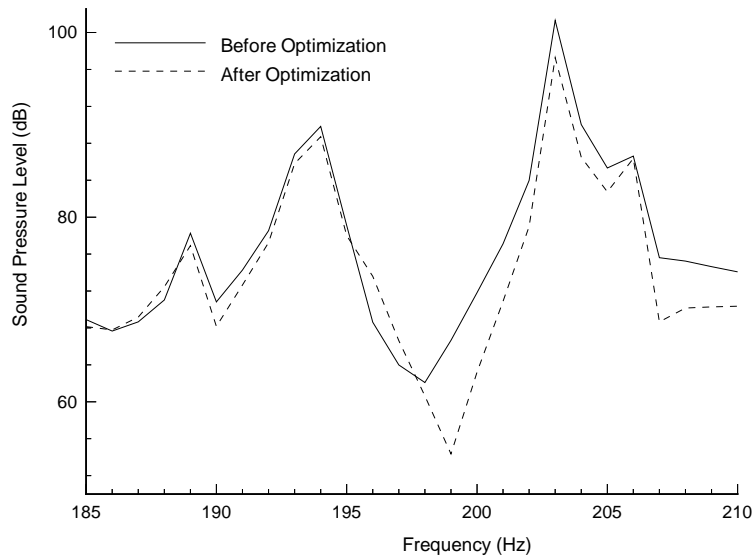


Figure B25 Sound pressure level versus excitation frequency before and after lamination angle optimization. Shown is the optimization frequency range for the response location at the rear window on the starboard side of the aircraft.

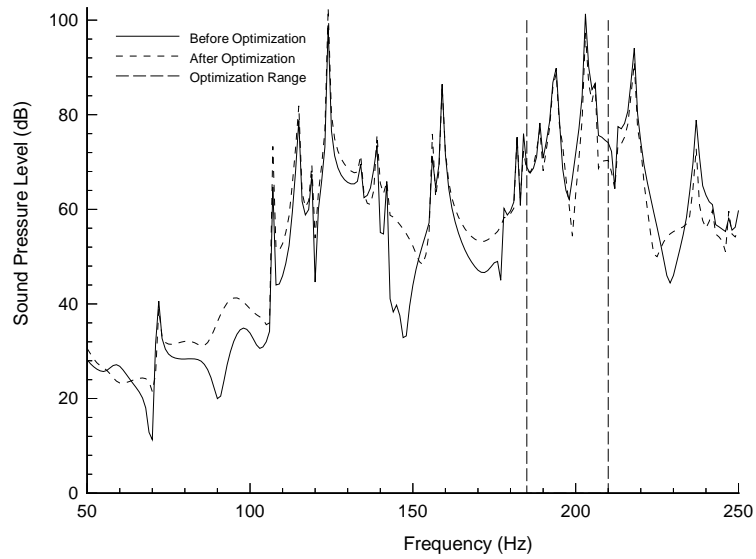


Figure B26 Sound pressure level versus excitation frequency before and after lamination angle optimization. Shown is the full excitation frequency range and the limits of the optimization range for the response location at the rear window on the starboard side of the aircraft.

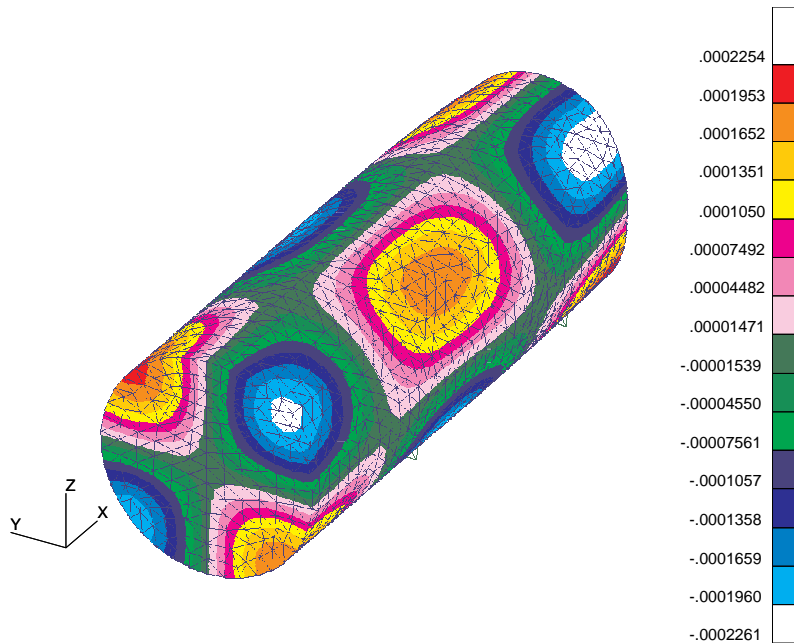


Figure B27 Acoustic pressure response in the passenger cabin at an excitation frequency of 203 Hz prior to lamination angle optimization.

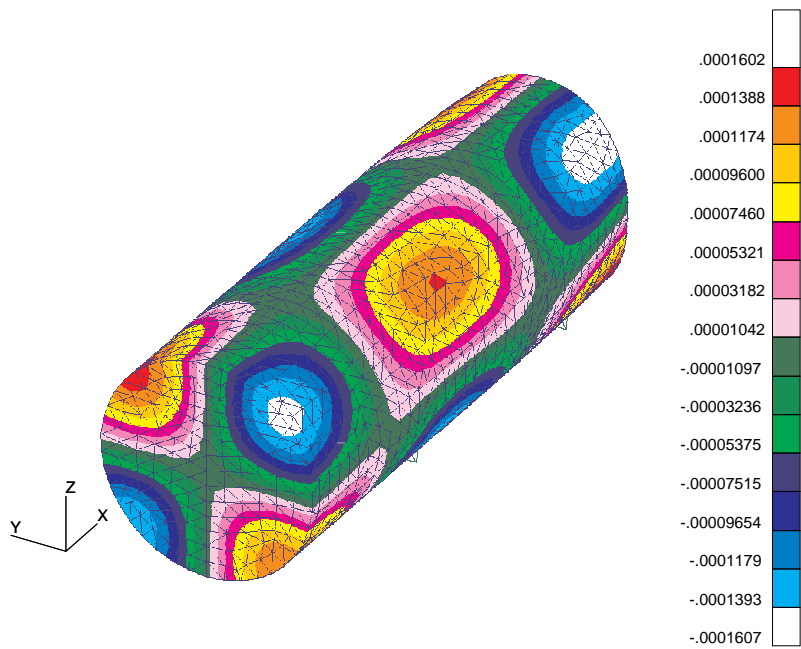


Figure B28 Acoustic pressure response in the passenger cabin at an excitation frequency of 203 Hz after lamination angle optimization.

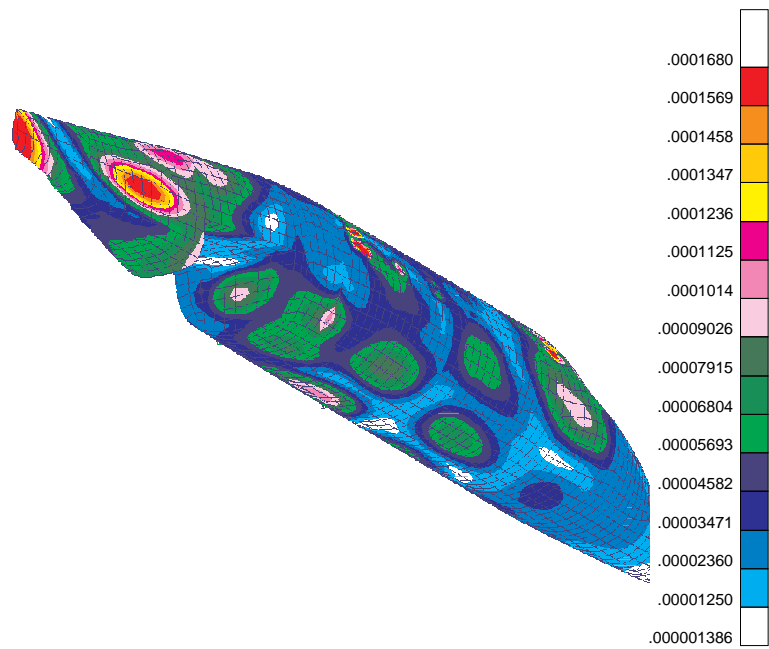


Figure B29 Structural displacement magnitudes at an excitation frequency of 203 Hz prior to lamination angle optimization.

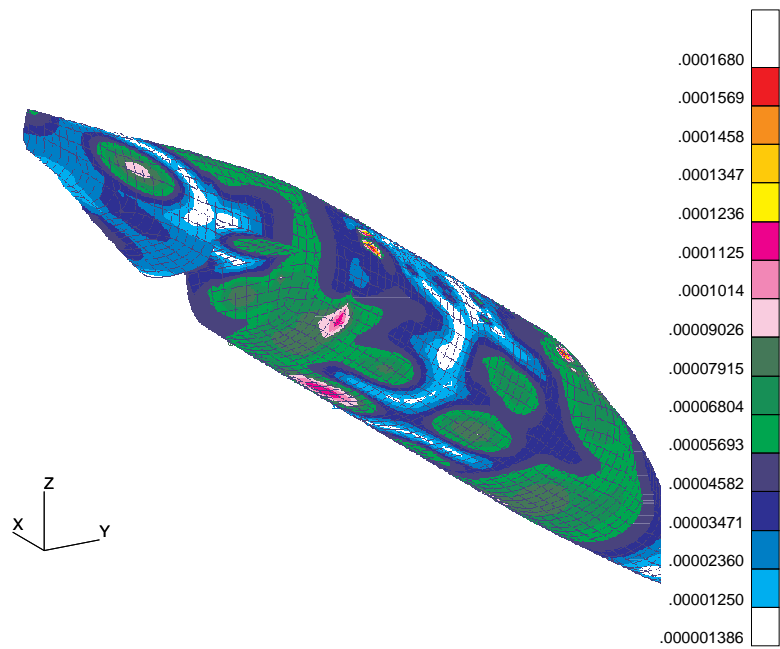


Figure B30 Structural displacement magnitudes at an excitation frequency of 203 Hz after lamination angle optimization.

Appendix C Sound Pressure Level at All Response Points for the Optimization Problem

This appendix presents the acoustic pressure response before and after optimization of the lamination angles at all ten response locations used for the optimization. Also included is a brief explanation of the coordinate system used for the model and a table of the (x,y,z) locations of the response points.

A Cartesian coordinate system was used to describe the locations of the nodes in the finite element model. The x-axis was aligned with the longitudinal (roll) axis of the aircraft and the z-axis was aligned with the vertical (yaw) axis of the Starship. The nose of the aircraft was located at the point (0,0,72). Additional points of reference in the model are listed in Table C1.

Reference Point	Flight Station (x-location, in.)
Nose of aircraft	0
Front of passenger cabin	170
Forward wing mounting brackets	237
Aft wing mounting brackets	324
Rear of passenger cabin	357
Forward bulkhead below baggage compartment	357
Aft bulkhead below baggage compartment	416
Tail of aircraft	537

Table C1 Table listing the flight stations (x-axis locations) of a number of geometrically significant points in the Starship finite element model. Stations are listed in inches.

A total of ten fluid nodes were used as response locations for the optimization problem. These grids were chosen to represent the approximate listening locations of

the passengers within the cabin. Table C2 provides a listing of the (x,y,z) locations for each of these nodes.

Node Description	x-coordinate	y-coordinate	z-coordinate
First window, port side	220.3	-15.6	122.3
First window, starboard side	221.50	15.2	125.6
Second window, port side	249.7	-12.4	123.3
Second window, starboard side	250.5	14.9	125.14
Third window, port side	282.8	-22.6	124.9
Third window, starboard side	279.1	16.8	120.8
Fourth window, port side	310.1	-19.8	122.5
Fourth window, starboard side	312.5	13.22	124.7
Fifth window, port side	337.3	-15.5	122.9
Fifth window, starboard side	339.6	19.9	119.7

Table C2 Table of response node locations in the model. Locations are in inches.

Figures C1 through C10 show the acoustic pressure response verses excitation frequency for each of the nodes in Table C2. The responses before and after optimization and the frequency range of optimization are also shown.

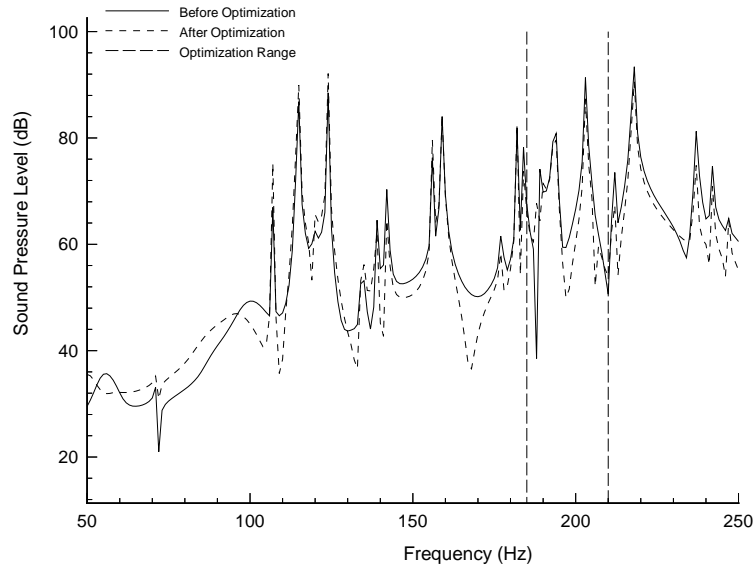


Figure C1 Sound pressure level before and after optimization for the response location at the first window on the port side of the aircraft. The peak response has been reduced by 4.01 dB.

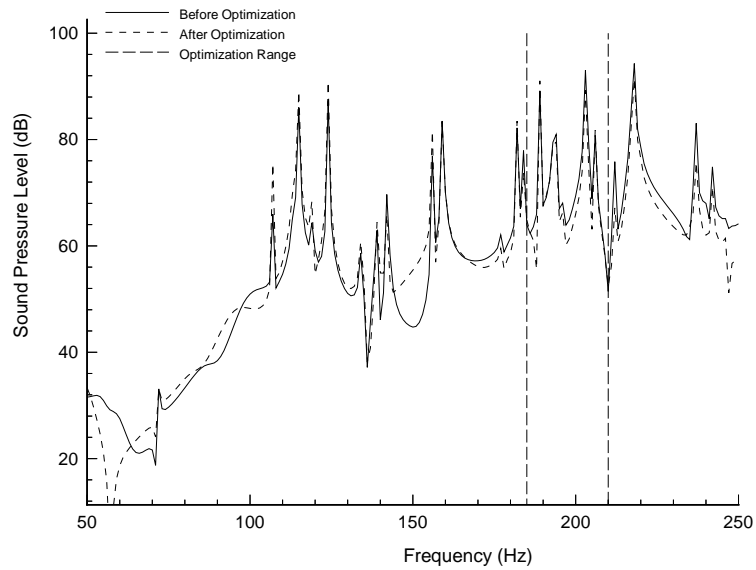


Figure C2 Sound pressure level before and after optimization for the response location at the first window on the starboard side of the aircraft. The peak response has been reduced by 3.81 dB.

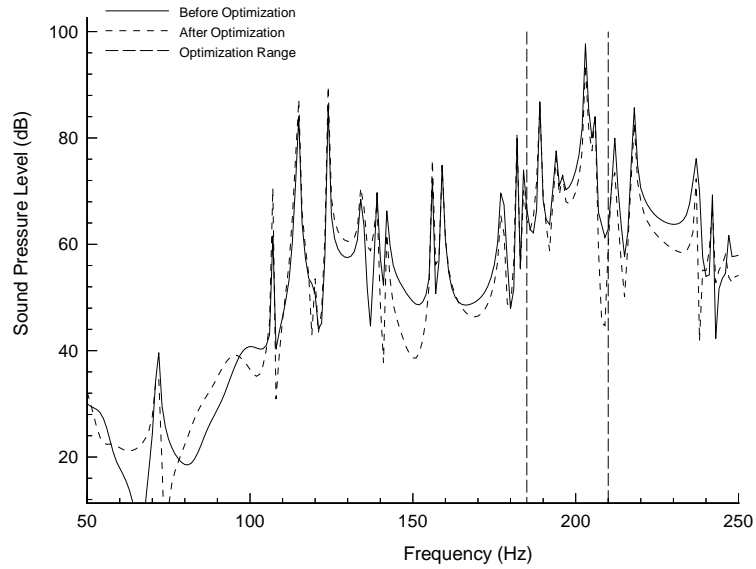


Figure C3 Sound pressure level before and after optimization for the response location at the second window on the port side of the aircraft. The peak response has been reduced by 3.96 dB.

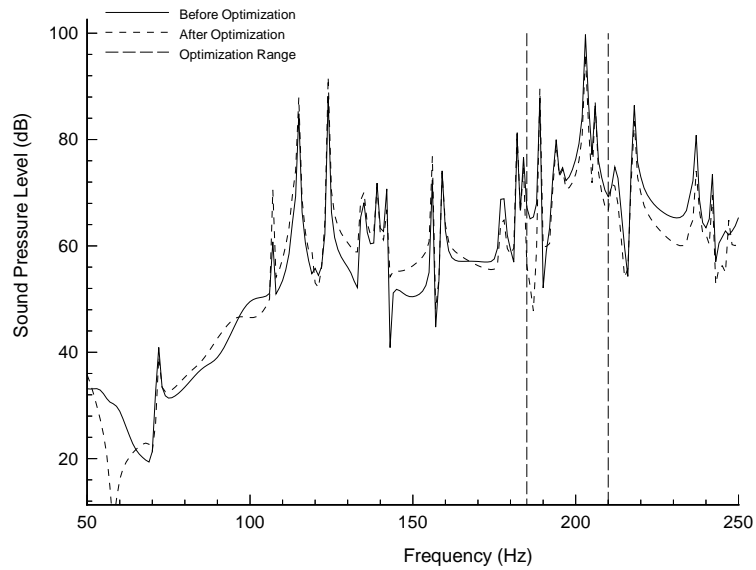


Figure C4 Sound pressure level before and after optimization for the response location at the second window on the starboard side of the aircraft. The peak response has been reduced by 3.79 dB.

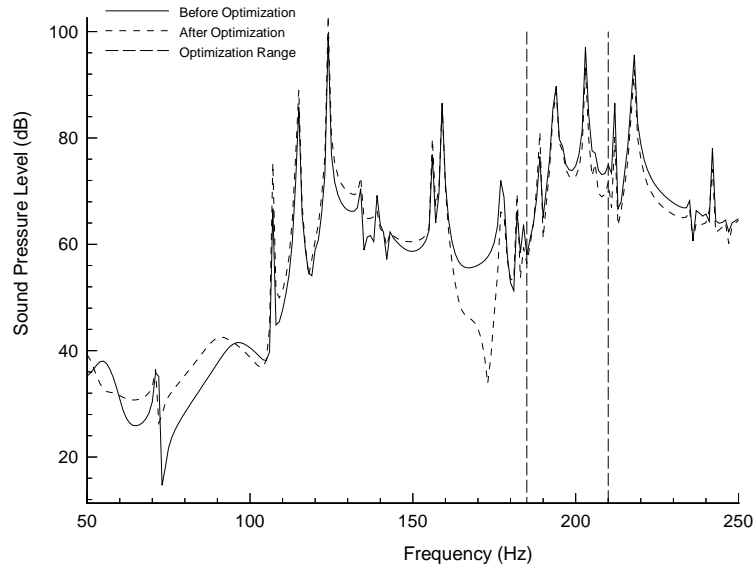


Figure C5 Sound pressure level before and after optimization for the response location at the third window on the port side of the aircraft. The peak response has been reduced by 3.76 dB.

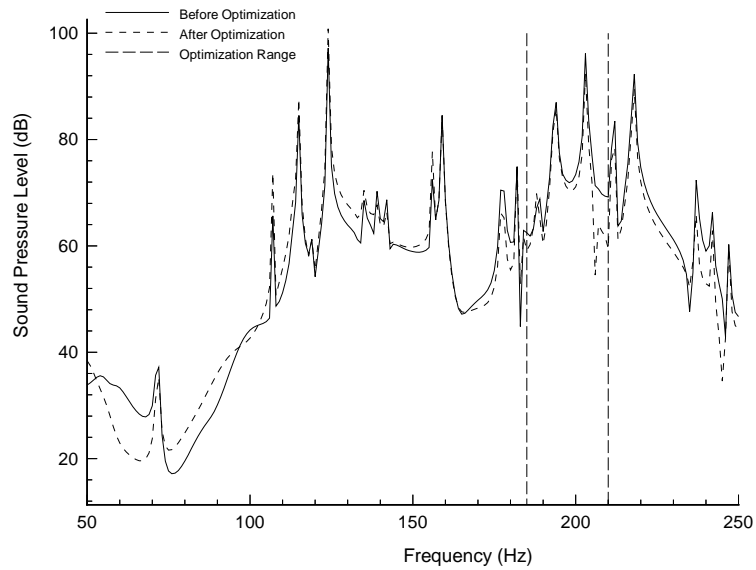


Figure C6 Sound pressure level before and after optimization for the response location at the third window on the starboard side of the aircraft. The peak response has been reduced by 3.77 dB.

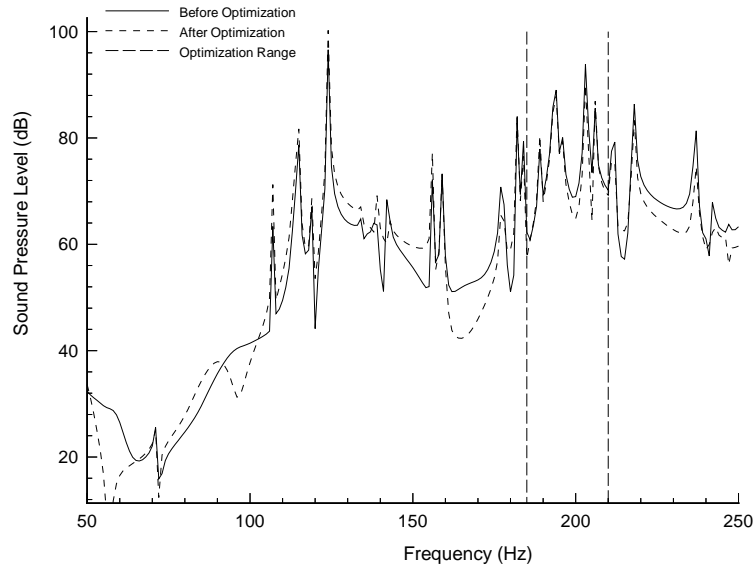


Figure C7 Sound pressure level before and after optimization for the response location at the fourth window on the port side of the aircraft. The peak response has been reduced by 4.07 dB.

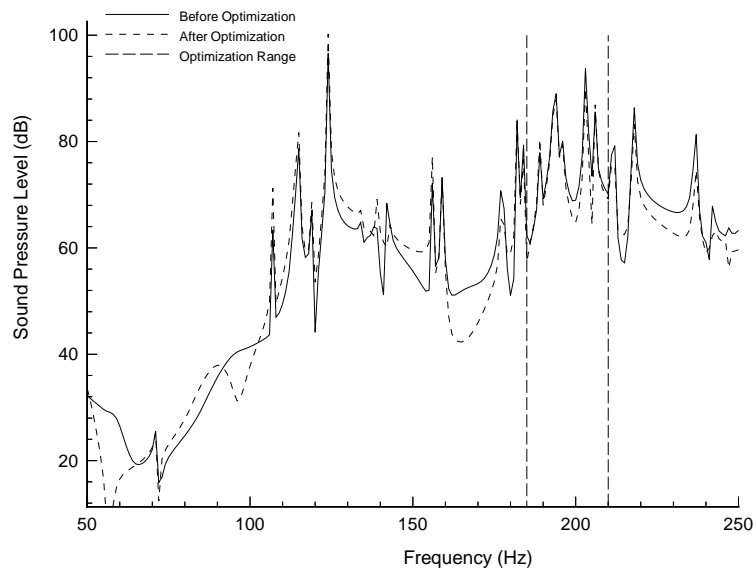


Figure C8 Sound pressure level before and after optimization for the response location at the fourth window on the starboard side of the aircraft. The peak response has been reduced by 3.85 dB.

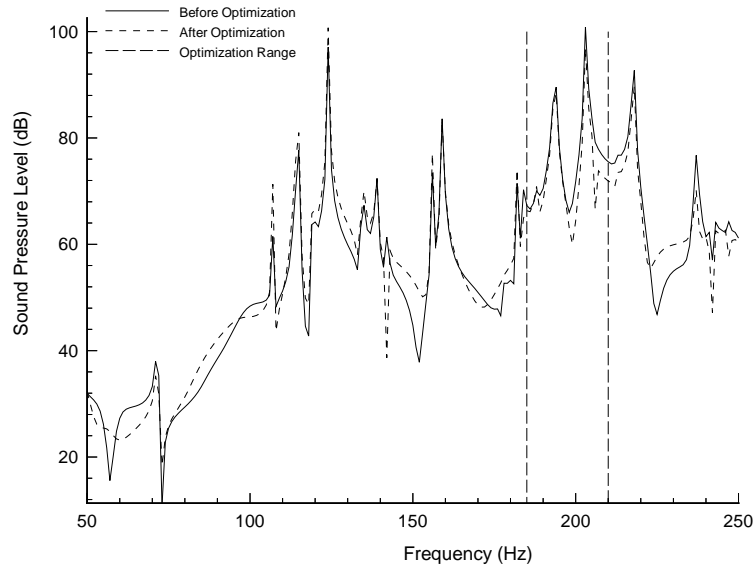


Figure C9 Sound pressure level before and after optimization for the response location at the fifth window on the port side of the aircraft. The peak response has been reduced by 3.97 dB.

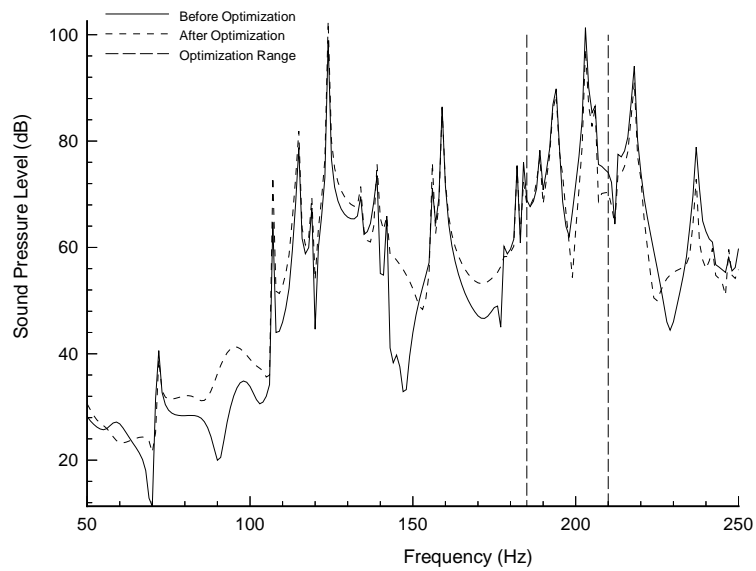


Figure C10 Sound pressure level before and after optimization for the response location at the fifth window on the starboard side of the aircraft. The peak response has been reduced by 4.03 dB.

Appendix D Computer Codes

This appendix contains a source code listing of the FORTRAN and *Mathematica*⁴ programs written in support of this work. Also included in this Appendix is a portion of the MSC/NASTRAN bulk data file showing the structure of the optimization used for the present work. The codes listed in this Appendix have been written specifically for this study and should be considered to be research code only. They are provided for completeness. Their successful operation cannot be guaranteed outside the scope of the present work.

D.1: FORTRAN Program compfreq.f

This is a program written in the FORTRAN language and it was used in the present work to calculate the forced frequency response of the fluid/structure cylinder in Chapter 3. This code makes calls to Bessel function algorithms. These algorithms can be found in the literature [35]. The structure is assumed to be specially orthotropic and the fluid is ideal. Material properties for the structure are read from the file “layers.dat”. The Donnell-Mushtari theory is used to describe the motion of the cylinder. The cylinder displacements are coupled to the fluid in the cylinder. However, the fluid backpressure is not coupled to the structure.

As outlined in Appendix A, the boundary conditions applied to the structure are those for a simple support. Boundary conditions of $p=0$ are applied to the fluid endcaps of the system. The natural vibration frequencies for the structure can be output to a separate file.

⁴ *Mathematica* is a registered trademark of Wolfram Research, Inc.

```

      program compfreq
c
c Program to calculate the natural frequencies of free vibration
c for a laminated orthotropic cylindrical shell and the forced
c frequency response. The shell contains an ideal fluid (air) and the
c acoustic response of this fluid to the vibration of the shell is
c determined. Boundary conditions are those of simple support,
c with no constraints in the axial direction.
c
c Input files include layers.dat, a file which contains data about
c the number of lamina in the shell and the material properties for
c each.
c
c Output files include:
c freq.out, a file which contains the mode numbers and natural
c frequencies of the cylinder.
c disp.out, contains displacement information at a point on the shell
c and acoustic pressure information at a point in the fluid.
c
c Declarations
c
      implicit real(a-h,o-y)
      implicit complex(z)
      real l,lam,nu12,nu21,hh,kk
c
      character*15 infile
c
      parameter (pi=3.141592654,maxf=150,moden=40,modem=40)
c
      dimension C(4,3,3),A(3,3),DS(3,3),D(3,3),h(4,2),
&              u(maxf),v(maxf),w(maxf),p(maxf),frequency(maxf)
c
      logical print
c
c Begin program
c
      zi=cplx(0.0,1.0)
c
c Specify geometry of the shell
c
      l=164.0
      r=35.0
      rzero=0.0
      small=10.0E-25
c
c Density of the fluid (air) (slugs/in**3)
      rhof=1.17e-7
c Acoustic speed of sound (in/sec)
      co=13620.0
c Structural damping
      eta=0.0
c Applied force (lbs.)
      Fo=0.3
c Acoustic reference pressure (psi)
      pref=2.9e-9
c
c Specify location of interest (tt in radians)
c
      rr=34.99991502
      tt=1.1781
      yz=(23.4285)/r
c
c Frequency increment (Hz)
      step=1.0
c Starting frequency
      freq=1.0*(2.0*pi)
c Print natural frequencies once
      print=.FALSE.
c Input file
      infile="layers.dat"
c

```

```

do 50 i=1,3
do 55 j=1,3
    A(i,j)=0.0
    D(i,j)=0.0
    DS(i,j)=0.0
55 continue
50 continue
c
c Get material properties from layers.dat file
c
    open(unit=10,file=infile,status='old')
c
    read(10,1000)layers
c
    do 100 k=1,layers
        read(10,*)E11,E22,nu12,nu21,G
        write(*,*)E11,E22,nu12,nu21,G
        read(10,*)hh,rhos
        write(*,*)hh,rhos
100 continue
c
    close(10)
    pause
c
c Prepare tecplot natural frequencies output file
    if (print) then
        open(unit=20,file='freq.out',status='unknown')
        write(20,1005)'TITLE = "Variation of Frequency with m"'
        write(20,1005)'VARIABLES = "m","n","w_1","w_2","w_3"'
    endif
c
c Prepare tecplot displacement output file
    open(unit=30,file='disp.out',status='unknown')
    write(30,1005)'TITLE="Forced Fluid/Structure Cylinder Resp."'
    write(30,1005)'VARIABLES="Freq","u","v","w","p"'
    write(30,1005)'ZONE T="Analytic"'
c
do 305 k=1,maxf
c
    zu=cplx(0.0,0.0)
    zv=cplx(0.0,0.0)
    zw=cplx(0.0,0.0)
    zp=cplx(0.0,0.0)
c
do 300 n=0,moden
c
    if (print) write(20,1010)'ZONE T="n=',n,'"
c
do 350 m=1,modem
c
    lam=(m*pi*r)/l
    kk=hh*hh/(12.0*r*r)
c
c Calculate alpha's
c
    p11=(-lam*lam-n*n*(G*(1.0-nu12*nu21)/E11))
    p12=lam*n*((nu12*E22+G*(1.0-nu12*nu21))/E11)
    p13=lam*nu12*E22/E11
    p21=lam*n*((nu12*E22+G*(1.0-nu12*nu21))/E11)
    p22=-lam*lam*(G*(1.0-nu12*nu21)/E11)-n*n*E22/E11
    p23=-n*E22/E11
    p31=-lam*nu12*E22/E11
    p32=n*E22/E11
    p33=E22/E11+kk*(lam*lam*lam*lam+2.0*n*lam*lam*
& ((nu12*E22+2.0*G*(1.0-nu12*nu21))/E11)+(E22/E11)*
& n*n*n)
c
c Define cubic equation constants
c
    C1= (p11+p22-p33)
    C2= (p11*p22-p11*p33-p22*p33+p23*p32-p12*p21+p13*p31)

```

```

      C3= (p11*(p23*p32-p22*p33)+p12*(p21*p33-p23*p31)+
&        p13*(p31*p22-p21*p32))
c
c   Solve equation for omega squared.
c
      cc=(1.0/3.0)*(3.0*C2-C1*C1)
      dd=(1.0/27.0)*(2.0*C1*C1*C1-9.0*C1*C2+27.0*C3)
c
      delta=(dd*dd/4.0)+(cc*cc*cc/27.0)
c
      if (delta.LT.0.0) then
        partone=-dd/2.0
        parttwo=SQRT(-1.0*delta)
        zPP=cmplx(partone,parttwo)
        zQQ=cmplx(partone,-parttwo)
      else
        partone=-dd/2.0
        parttwo=SQRT(delta)
        zPP=cmplx((partone+parttwo),rzero)
        zQQ=cmplx((partone-parttwo),rzero)
      endif
c
      zPP=zPP**(1.0/3.0)
      zQQ=zQQ**(1.0/3.0)
c
      zfirst=-0.5*(zPP+zQQ)
      zsecnd=-0.5*(zPP-zQQ)*SQRT(3.0)*zi
c
      partone=real(zfirst)+real(zsecnd)
      parttwo=imag(zfirst)+imag(zsecnd)
      parttre=real(zfirst)-real(zsecnd)
      partfor=imag(zfirst)-imag(zsecnd)
c
      zroot1=zPP+zQQ-C1/3.0
      zroot2=cmplx((partone-C1/3.0),parttwo)
      zroot3=cmplx((parttre-C1/3.0),partfor)
c
      zfreq1=SQRT(zroot1*E11/(rhos*r*r*(1-nu12*nu21)))
      zfreq2=SQRT(zroot2*E11/(rhos*r*r*(1-nu12*nu21)))
      zfreq3=SQRT(zroot3*E11/(rhos*r*r*(1-nu12*nu21)))
c
      if (imag(zfreq1).NE.0.0.OR.
&        imag(zfreq2).NE.0.0.OR.
&        imag(zfreq3).NE.0.0) then
        write(*,1005)'Warning: Non-zero imaginary frequency'
      endif
c
      if (print) then
        write(20,1015)m,n,real(zfreq1/(2.0*pi)),
&          real(zfreq2/(2.0*pi)),
&          real(zfreq3/(2.0*pi))
        if (n.EQ.moden) then
          close(20)
          print=.FALSE.
        endif
      endif
c
c   Output for non-dimensional parameters
c
      if (print) then
        x=lam/pi
        zout1=SQRT(zroot1)
        zout2=SQRT(zroot2)
        zout3=SQRT(zroot3)
        write(20,1020)x,n,real(zout1),
&          real(zout2),
&          real(zout3)
        if (n.EQ.modes) close(20)
      endif
c
      call magnitude(zfreq1,freq1)

```

```

        call magnitude(zfreq2,freq2)
        call magnitude(zfreq3,freq3)
c
        Cls=E11/(rhos*(1.0-nu12*nu21))
c
c Calculate force coefficient
c
        Fmn=r*(2.0/(pi*1))*Fo*sin(m*pi/2.0)*(1.0+cos(n*pi))
c
        rootA=-SQRT(-(Cls/(r*r))*(lam*lam*G*(nu12*nu21-1.0)+
&                n*n*(E22-E11+G*(1.0/nu12-nu21)))/E11)
c
        rootB=-SQRT(-(Cls/(r*r))*(lam*lam*(nu12*nu12*E22-E11+
&                nu12*G*(1.0-nu12*nu21))+n*n*G*(nu12*nu21-1.0))/
&                E11)
c
        beta =(Cls/(r*r))*(lam*lam+n*n*G*(1.0-nu12*nu21)/E11)
        gamma=(Cls/(r*r))*(lam*lam*G*(1.0-nu12*nu21)/E11+n*n*E22/E11)
        xi   =(Cls/(r*r))*(lam*n*nu12*E22+G*(1.0-nu12*nu21))/E11
c
        discr=SQRT((beta+gamma)*(beta+gamma)+4.0*(xi*xi-beta*gamma))
c
        omegaC=0.5*((beta+gamma)+discr)
        omegaD=0.5*((beta+gamma)-discr)
c
        rootC=SQRT(omegaC)
        rootD=SQRT(omegaD)
c
        zdet=cmplx((freq*freq-freq3*freq3),2.0*eta*freq*freq3)*
&          cmplx((freq*freq-freq2*freq2),2.0*eta*freq*freq2)*
&          cmplx((freq*freq-freq1*freq1),2.0*eta*freq*freq1)
c
        zcofA=cmplx((freq*freq-rootA*rootA),2.0*eta*freq*rootA)
        zcofB=cmplx((freq*freq-rootB*rootB),2.0*eta*freq*rootB)
        zcofC=cmplx((freq*freq-rootC*rootC),2.0*eta*freq*rootC)*
&          cmplx((freq*freq-rootD*rootD),2.0*eta*freq*rootD)
c
        zAmn=- (Fmn/(rhos*hh))*zcofA/zdet*1.0/(r*r)
        zBmn=- (Fmn/(rhos*hh))*zcofB/zdet*1.0/(r*r)
        zCmn=- (Fmn/(rhos*hh))*zcofC/zdet*1.0/(r*r)
c
c Sum displacements
c
        zu=zu+zAmn*cos(lam*yz)*cos(n*tt)
        zv=zv+zBmn*sin(lam*yz)*sin(n*tt)
        zw=zw+zCmn*sin(lam*yz)*cos(n*tt)
c
c Solve for pressure coefficient
c
        alphasqr=(freq*freq)/(co*co)-lam*lam/(r*r)
c
        if (alphasqr.LT.0.0) then
            alph=SQRT(-1.0*alphasqr)
            call cofimag(small,r,alph,n,bottom)
            zDmn=(zCmn*rhof*freq*freq)/bottom
            call bessimag(small,rr,alph,n,press)
        elseif (alphasqr.GT.0.0) then
            alph=SQRT(alphasqr)
            call realcof(small,r,alph,n,bottom)
            zDmn=(zCmn*rhof*freq*freq)/bottom
            call bessreal(small,rr,alph,n,press)
        elseif (alphasqr.EQ.0.0) then
            write(*,*)'Alpha = 0.0'
        endif
c
c Sum pressure
c
        zp=zp+zDmn*press*sin(lam*yz)*cos(n*tt)
c
350 continue

```

```

300 continue
c
c Dummy print
  write(*,*)'Complex pressure = ',zp
  write(*,1)'Complex data calculated for ',k
c
c Convert complex displacements, pressure to magnitudes
c
  call magnitude(zu,u(k))
  call magnitude(zv,v(k))
  call magnitude(zw,w(k))
c
c Convert pressure to dB scale
  call magnitude(zp,p(k))
  p(k)=20.0*(0.4342944819*log(p(k)/pref))
c
c Write to tecplot file
c
  frequency(k)=freq/(2.0*pi)
  write(30,1025)frequency(k),10.0E-10,v(k),w(k),p(k)
c
c Increment frequency
  freq=freq+step*(2.0*pi)
c
305 continue
c
  close(30)
c
1   format(a28,i4)
1000 format(i2)
1005 format(a)
1010 format(a10,i2,a1)
1015 format(i3,1x,i3,3(1x,f12.2))
1020 format(f12.6,1x,i3,3(1x,f12.6))
1025 format(f7.2,4(1x,e16.9))
c
  stop
  end
c
c *****
c   subroutine magnitude(z,x)
c
c   Subroutine to return the magnitude x of a complex argument z
c
  implicit real(a-h,o-y)
  implicit complex(z)
c
  partone=real(z)
  parttwo=imag(z)
c
  x=SQRT(partone*partone+parttwo*parttwo)
c
  return
  end
c
c *****
c   subroutine realcof(tiny,a,alph,n,out)
c
c   Subroutine to return the denominator of the pressure coefficient term.
c   Used when the argument of the n-th order bessel function is real.
c
  implicit real(a-h,o-y)
  implicit complex(z)
c
  zi=cmplx(0.0,1.0)
c
  x=alph*a
c
  if (n.EQ.0) then
    term1=BESSJ0(x)
    term2=BESSJ1(x)

```

```

elseif (n.EQ.1) then
    term1=BESSJ1(x)
    term2=BESSJ(2,x)
else
    term1=BESSJ(n,x)
    term2=BESSJ((n+1),x)
endif
c
c out=(n/a)*term1-alph*term2
c
c if (ABS(out).LT.tiny) then
c   if (out.LT.0.0) then
c     out=-1.0*tiny
c   else
c     out=tiny
c   endif
c
c endif
c return
c end
c
c *****
c   subroutine cofimag(tiny,a,alpha,n,out)
c
c Subroutine to return the denominator of the pressure coefficient term.
c Used when the argument of the n-th order Bessel function is complex.
c
c   implicit real (a-h,o-y)
c   implicit complex(z)
c
c   x=alpha*a
c
c   if (n.EQ.0) then
c     term1=BESSI0(x)
c     term2=BESSI1(x)
c   elseif (n.EQ.1) then
c     term1=BESSI1(x)
c     term2=BESSI(2,x)
c   else
c     term1=BESSI(n,x)
c     term2=BESSI((n+1),x)
c   endif
c
c   out=alpha*term2+(n/a)*term1
c
c   if (ABS(out).LT.tiny) then
c     if (out.LT.0.0) then
c       out=-1.0*tiny
c     else
c       out=tiny
c     endif
c   endif
c
c   return
c   end
c
c *****
c   subroutine bessreal(tiny,r,alpha,n,out)
c
c Subroutine to return the n-th order bessel function of a real argument.
c
c   implicit real (a-h,o-y)
c   implicit complex (z)
c
c   x=r*alpha
c
c   if (n.EQ.0) then
c     out=BESSJ0(x)
c   elseif (n.EQ.1) then
c     out=BESSJ1(x)
c   else

```

```

        out=BESSJ(n,x)
    endif
c
    if (ABS(out).LT.tiny) then
        if (out.LT.0.0) then
            out=-1.0*tiny
        else
            out=tiny
        endif
    endif
c
    return
end

c
c *****
c      subroutine bessimag(tiny,r,alpha,n,out)
c
c      Subroutine to return the n-th order modified bessel function of a real
c      argument.
c
c      implicit real (a-h,o-y)
c      implicit complex (z)
c
c      x=r*alpha
c
c      if (n.EQ.0) then
c          out=BESSI0(x)
c      elseif (n.EQ.1) then
c          out=BESSI1(x)
c      else
c          out=BESSI(n,x)
c      endif
c
c      if (ABS(out).LT.tiny) then
c          if (out.LT.0.0) then
c              out=-1.0*tiny
c          else
c              out=tiny
c          endif
c      endif
c
c      return
end

```

D.2: *Mathematica*TM program sensitivity.m

This computer code was written for use by the *Mathematica*TM computer mathematics program [36]. Like the compfreq.f program (above), it calculates the displacements of the thin, cylindrical shell and the acoustic pressure inside the shell. This code also calculates the sensitivities of the shell structural displacement and the acoustic response to changes in lamination angle in the structure.

The solution outlined in Appendix A is again used to describe the motion of the cylinder. However, this solution is only valid for lamination angles near 0° or 90°;

i.e. angles where the material becomes specially orthotropic. Therefore, the sensitivities calculated by this code are approximations valid only near either of these two angles.

```
(*Mathematica program to determine radial displacement of a circular,
cylindrical shell using the Love-Timoshenko anisotropic operator.
Acoustic pressure at an interior point of the cylinder is also calculated
Sensitivity of these values WRT lamination angle psi near psi=0 is
determined. *)
(**)
LT={{ {lt11,lt12,lt13}, {lt21,lt22,lt23}, {lt31,lt32,lt33}}
pv={0,0,Fmn}
(**)
(* Define general solution *)
u=Cos[lam*s]*Cos[n*th]
v=Sin[lam*s]*Sin[n*th]
w=Sin[lam*s]*Cos[n*th]
(**)
(* Define circular cylinder geometry *)
h=0.174
a=35.0
l=164.0
pi=3.141592654
(**)
(* Define material properties *)
E11=30.0*10^6
E22=0.75*10^6
nu12=0.25
nu21=0.00625
G12=0.375*10^6
rho=1.458*10^-4
(* Define fluid properties *)
rhof=1.17*10^-7
cnot=13620.0
pref=2.9*10^-9
(**)
(* Define A, B, and D matrices *)
AA={{ {A11,A12,A16}, {A12,A22,A26}, {A16,A26,A66}}
A11=h*QB11
A12=h*QB12
A16=h*QB16
A22=h*QB22
A26=h*QB26
A66=h*QB66
(*BB={{ {B11,B12,B16}, {B12,B22,B26}, {B16,B26,B66}}
B11=0.5*h*h*QB11
B12=0.5*h*h*QB12
B16=0.5*h*h*QB16
B22=0.5*h*h*QB22
B26=0.5*h*h*QB26
B66=0.5*h*h*QB66*)
DD={{ {D11,D12,D16}, {D12,D22,D26}, {D16,D26,D66}}
D11=(1/12)*h*h*h*QB11
D12=(1/12)*h*h*h*QB12
D16=(1/12)*h*h*h*QB16
D22=(1/12)*h*h*h*QB22
D26=(1/12)*h*h*h*QB26
D66=(1/12)*h*h*h*QB66
(**)
(* Define the reduced stiffnesses Qij (Jones p 46) *)
Q11=E11/(1-nu12*nu21)
Q12=nu12*E22/(1-nu12*nu21)
Q22=E22/(1-nu12*nu21)
Q66=G12
(**)
(* Define global reduced stiffnesses Qij-bar (Jones p 51) *)
QB11=Q11*(Cos[psi])^4+2*(Q12+2*Q66)*Sin[psi]*Sin[psi]*Cos[psi]*Cos[psi]+
Q22*(Sin[psi])^4
QB12=(Q11+Q22-4*Q66)*Sin[psi]*Sin[psi]*Cos[psi]*Cos[psi]+Q12*((Sin[psi])^4+
(Cos[psi])^4)
```

```

QB22=Q11*(Sin[psi])^4+2*(Q12+2*Q66)*Sin[psi]*Sin[psi]*Cos[psi]*Cos[psi]+
Q22*(Cos[psi])^4
QB16=(Q11-Q12-2*Q66)*Sin[psi]*Cos[psi]*Cos[psi]*Cos[psi]+
(Q12-Q22+2*Q66)*Sin[psi]*Sin[psi]*Sin[psi]*Cos[psi]
QB26=(Q11-Q12-2*Q66)*Sin[psi]*Sin[psi]*Sin[psi]*Cos[psi]+
(Q12-Q22+2*Q66)*Sin[psi]*Cos[psi]*Cos[psi]*Cos[psi]
QB66=(Q11+Q22-2*Q12-2*Q66)*Sin[psi]*Sin[psi]*Cos[psi]*Cos[psi]
+Q66*((Sin[psi])^4+(Cos[psi])^4)
(* Define Donnell-Mushtari anisotropic operator *)
k=(h*h)/(12*a*a)
lt11=(A11/A22)*D[D[u,s],s]+2*(A16/A22)*D[D[u,s],th]+(A66/A22)*D[D[u,th],th]+
u*(a*a*h*rho/A22)*om
lt12=(A16/A22)*D[D[v,s],s]+((A12+A66)/A22)*D[D[v,s],th]+(A26/A22)*D[D[v,th],th]
lt13=(A12/A22)*D[w,s]+(A26/A22)*D[w,th]
lt22=(A66/A22)*D[D[v,s],s]+2*(A26/A22)*D[D[v,s],th]+D[D[v,th],th]+
v*(a*a*h*rho/A22)*om
lt23=(A26/A22)*D[w,s]+D[w,th]
lt33=w+k*((D11/D22)*D[D[D[w,s],s],s]+
2*((D12+2*D66)/D22)*D[D[D[w,s],s],th]+D[D[D[w,th],th],th])-
w*(a*a*h*rho/A22)*om
lt21=(A16/A22)*D[D[u,s],s]+((A12+A66)/A22)*D[D[u,s],th]+(A26/A22)*D[D[u,th],th]
lt31=(A12/A22)*D[u,s]+(A26/A22)*D[u,th]
lt32=(A26/A22)*D[v,s]+D[v,th]
(**)
(* Add Love-Timoshenko modifier *)
lt22=lt22+k*(2*(D66/D22)*D[D[v,s],s]+3*(D26/D22)*D[D[v,s],th]+D[D[v,th],th])
lt23=lt23-k*((D16/D22)*D[D[D[w,s],s],s]+((D12+2*D66)/D22)*D[D[D[w,s],s],th]+
3*(D26/D22)*D[D[D[w,s],th],th]+D[D[D[w,th],th],th])
lt32=lt32-k*(2*(D16/D22)*D[D[D[v,s],s],s]+((D12+4*D66)/D22)*D[D[D[v,s],s],th]+
4*(D26/D22)*D[D[D[v,s],th],th]+D[D[D[v,th],th],th])
lt33=lt33+k*(4*(D16/D22)*D[D[D[w,s],s],s]+
4*(D26/D22)*D[D[D[w,s],s],th])
(**)
(* Compute acoustic pressure *)
p=Sin[lam*s]*Cos[n*th]*BesselJ[n,alpha*rad]
lower=D[BesselJ[n,(alpha*rbound)],rbound]
alpha=SQRT(om/(cnot*cnot)-(m*pi)*(m*pi)/(l*1))
rbound=a
(**)
(* Define applied forced vector *)
cf=1/A22
Fmn=fo*cf*sin[m*pi/2]*(1+cos[n*pi])*(2*a/(pi*1))
fo=0.3
(**)
(* Define derivatives of the LT matrix WRT psi (lamination angle)*)
dlt11=D[lt11,psi]
dlt12=D[lt12,psi]
dlt13=D[lt13,psi]
(**)
dlt21=D[lt21,psi]
dlt22=D[lt22,psi]
dlt23=D[lt23,psi]
(**)
dlt31=D[lt31,psi]
dlt32=D[lt32,psi]
dlt33=D[lt33,psi]
(**)
(* Remove trig terms from operator *)
t11=Simplify[Expand[lt11/u]]
t12=Simplify[Expand[lt12/u]]
t13=Simplify[Expand[lt13/u]]
t21=Simplify[Expand[lt21/v]]
t22=Simplify[Expand[lt22/v]]
t23=Simplify[Expand[lt23/v]]
t31=Simplify[Expand[lt31/w]]
t32=Simplify[Expand[lt32/w]]
t33=Simplify[Expand[lt33/w]]
(**)
(* Define lamination angle psi *)
psi=0.0
(**)

```

```

lt11=Simplify[t11]
lt12=Simplify[t12]
lt13=Simplify[t13]
lt21=Simplify[t21]
lt22=Simplify[t22]
lt23=Simplify[t23]
lt31=Simplify[t31]
lt32=Simplify[t32]
lt33=Simplify[t33]
(**)
dlt11=Expand[dlt11]
dlt12=Expand[dlt12]
dlt13=Expand[dlt13]
dlt21=Expand[dlt21]
dlt22=Expand[dlt22]
dlt23=Expand[dlt23]
dlt31=Expand[dlt31]
dlt32=Expand[dlt32]
dlt33=Expand[dlt33]
t11=Simplify[dlt11]
t12=Simplify[dlt12]
t13=Simplify[dlt13]
t21=Simplify[dlt21]
t22=Simplify[dlt22]
t23=Simplify[dlt23]
t31=Simplify[dlt31]
t32=Simplify[dlt32]
t33=Simplify[dlt33]
DLT={{dlt11,dlt12,dlt13},{dlt21,dlt22,dlt23},{dlt31,dlt32,dlt33}}
(**)
(* Specify structural location of interest *)
th=75.61*(pi/180)
s=(35.1428)*(1/a)
lam=(m*pi*a/l)
(* Specify fluid location of interest *)
rad=30.67
(**)
dlt11=Simplify[t11]
dlt12=Simplify[t12]
dlt13=Simplify[t13]
dlt21=Simplify[t21]
dlt22=Simplify[t22]
dlt23=Simplify[t23]
dlt31=Simplify[t31]
dlt32=Simplify[t32]
dlt33=Simplify[t33]
(**)
LT={{lt11,lt12,lt13},{lt21,lt22,lt23},{lt31,lt32,lt33}}
DLT={{dlt11,dlt12,dlt13},{dlt21,dlt22,dlt23},{dlt31,dlt32,dlt33}}
pv={0,0,Fmn}
(**)
(*Define minor determinant for the 3-3 term in the LT matrix*)
coflt33=lt11*lt22-lt21*lt12
(*Define derivative of dlt33 minor determinant*)
dc=Expand[dlt11*lt22+dlt22*lt11-dlt21*lt12-dlt12*lt21]
dcoflt33=Simplify[dc]
(**)
(*Define derivative of the determinant LT*)
ddlt=dlt11*(lt22*lt33-lt23*lt32)+dlt12*(lt23*lt31-lt33*lt21)+
      dlt13*(lt21*lt32-lt22*lt31)+dlt21*(lt13*lt32-lt12*lt33)+
      dlt22*(lt11*lt33-lt13*lt31)+dlt23*(lt12*lt31-lt11*lt32)+
      dlt31*(lt12*lt23-lt13*lt22)+dlt32*(lt13*lt21-lt11*lt23)+
      dlt33*(lt11*lt22-lt12*lt21)
ds=Expand[ddlt]
ddlt=Simplify[ds]
(**)
(* Initialize output variables *)
out=0.0
dout=0.0
pout=0.0
sout=0.0

```

```

(**)
(* Open output file *)
OpenWrite["sens.out",PageWidth -> 164]
WriteString["sens.out","TITLE=\"Displacement Sensitivity to Ply Angle\\\"n"]
WriteString["sens.out","VARIABLES=\"Freq\\\", \"~6w/~6'y\\\", \"~6p/~6'y\\\", \"w\\\", \"p\\\"n"]
WriteString["sens.out","ZONE T=\"Analytic Sensitivity\\\"n"]
(**)
(* Determine D[Cmn,psi] - add mode shapes *)
Do[
Do[
lam=(m*pi*a/l);
dlt=Det[LT];
(* Compute displacement *)
Cmn=Fmn*cofl33/dlt;
out=out+Cmn*w;
(**)
(* Compute acoustic pressure *)
upper=Cmn*rhof*om;
Dmn=upper/lower;
pout=pout+Dmn*p;
(* Compute displacement sensitivity to lamination angle *)
first=Simplify[dcofl33*dlt];
second=Simplify[cofl33*ddl];
bottom=Simplify[dlt*dlt];
dout=dout+(pi/180)*Fmn*(first-second)/bottom;
sout=sout+(pi/180.0)*((rhof*om)/lower)*p*Fmn*(first-second)/bottom
,{m,1,15,2},{n,0,20,2}
(**)
om=f*f*4*pi*pi
Plot[Log[10,Abs[out]],{f,110,140},AxesLabel -> {"Freq","Log Displacement"}]
Plot[Log[10,Abs[dout]],{f,110,140},AxesLabel -> {"Freq","Log Disp Sens"}]
Plot[20*Log[10,Abs[pout/pref]],{f,110,140},AxesLabel -> {"Freq","Press (dB)"}]
Plot[Log[10,Abs[sout]],{f,110,140},AxesLabel -> {"Freq","Log Press Sens"}]*]
Do[
dummy=20.0*Log[10,Abs[pout/pref]];
qq=ToExpression["f"];
rr=ToExpression["Abs[out]"];
qr=ToExpression["dout"];
pp=ToExpression["dummy"];
pq=ToExpression["sout"];
Write["sens.out",qq,
OutputForm[" "],qr,
OutputForm[" "],pq,
OutputForm[" "],rr,
OutputForm[" "],pp,
{f,20,50,1}]
Close["sens.out"]

```

D.3: MSC/NASTRAN Bulk Data File

What follows is a portion of the MSC/NASTRAN bulk data file which was used for the optimization of the Starship fuselage in the present work. Shown is the formulation of the design variables, property relations, objective function and constraints for the problem. Not included in this listing is the finite element data for the model.

The design variables of the problem were normalized such that they varied between 1.0 and 2.0 with a starting point of 1.6. The design variables were related to the lamination angles of the composite through the DVPREL1 entries in the bulk data deck. The

objective function was defined using a DRESP2 card (number 100). The sound pressure levels at ten nodes in the fluid portion of the model were used as design constraints for the problem. For additional information regarding the bulk data cards referenced in this listing, the reader is referred to the literature [22, 37]

```

$ NASTRAN input file created by the PDA MSC/NASTRAN input file
$ translator ( PAT3/MSC-NASTRAN Release 1.4-2 ) on June      14, 1996 at
$ 15:11:49.
$ASSIGN OUTPUT2 = 'starship3.opt.op2', UNIT = 12, FORM = FORMATTED
$ Frequency Response Analysis, Direct Formulation, Database
$NASTRAN SYSTEM(146)=1,SYSTEM(196)=1
INIT SCRATCH LOGI=(SCRATCH(400000))
SOL 200
TIME 6000
CEND
SEALL = ALL
SUPER = ALL
$ Optimization case control
ANALYSIS = MFREQ
DESOBJ   = 100
DESSUB   = 500000
TITLE = MSC/NASTRAN job created on 04-Apr-96 at 11:18:01
ECHO = NONE
MAXLINES = 999999999
SET 777=12656,12645,13611,13728,14483,14455,15352,15454,16404,16410
SUBCASE 1
$ Subcase name : complete_loading
  SUBTITLE=complete_loading
  METHOD(structure) = 123
  METHOD(fluid)     = 213
  FREQUENCY = 1
  LOADSET = 1
  DLOAD = 2
  DISPLACEMENT(SORT1,PUNCH,REAL)=777
$ VELOCITY(SORT1,PUNCH,REAL)=777
BEGIN BULK
PARAM POST -1
PARAM PATVER 3.
PARAM AUTOSPC YES
PARAM PRGPST NO
PARAM COUPMASS 1
PARAM K6ROT 0.
PARAM WTMASS 1.
PARAM,NOCOMPS,-1
PARAM G 0.06
PARAM OPTEXIT 7
INCLUDE 'tet4.INC'
EIGRL 123 500 0
EIGRL 213 200 0
FREQ1 1 185. 1. 25
$ Elements and Element Properties for region : main-cabin
$ Composite Property Record created from P3/PATRAN composite material
$ record : MATRL.16
$ Composite Material Description : Created by neutral file import
PCOMP 7 -.4135 .06 + MU
+ MU 6 .0085 45. YES 10 .01 90. YES + MV
+ MV 10 .01 0. YES 10 .01 90. YES + MW
+ MW 5 .75 0. YES 10 .01 90. YES + MX
+ MX 10 .01 0. YES 10 .01 90. YES + MY
+ MY 6 .0085 45. YES
$ Optimization parameters
$ Define design variables (lamination angles, p-naught)
DESVAR 1 angle1 1.6 1.0 2.0 0.30
DESVAR 2 angle2 1.6 1.0 2.0 0.30
DESVAR 3 angle3 1.6 1.0 2.0 0.30

```

```

DESVAR 4 angle4 1.6 1.0 2.0 0.30
DESVAR 5 angle5 1.6 1.0 2.0 0.30
DESVAR 6 angle6 1.6 1.0 2.0 0.30
DESVAR 7 angle7 1.6 1.0 2.0 0.30
DESVAR 8 angle8 1.6 1.0 2.0 0.30
DESVAR 9 Po 100.0 40.0 150.0 0.15
$ Relate design variables to property values for main cabin region
DVPREL1 1 PCOMP 7 14 -225.0 + ZZZZZA
+ ZZZZZA 1 180.0
DVPREL1 2 PCOMP 7 18 -180.0 + ZZZZZB
+ ZZZZZB 2 180.0
DVPREL1 3 PCOMP 7 24 -90.0 -270.0 + ZZZZZC
+ ZZZZZC 3 180.0
DVPREL1 4 PCOMP 7 28 -180.0 + ZZZZZD
+ ZZZZZD 4 180.0
DVPREL1 5 PCOMP 7 38 -180.0 + ZZZZZE
+ ZZZZZE 5 180.0
DVPREL1 6 PCOMP 7 44 -90.0 -270.0 + ZZZZZF
+ ZZZZZF 6 180.0
DVPREL1 7 PCOMP 7 48 -180.0 + ZZZZZG
+ ZZZZZG 7 180.0
DVPREL1 8 PCOMP 7 54 -225.0 + ZZZZZH
+ ZZZZZH 8 180.0
$ Relate design variables to property values for main cabin doubler region
DVPREL1 11 PCOMP 4 14 -225.0 + ZAZZZA
+ ZAZZZA 1 180.0
DVPREL1 12 PCOMP 4 18 -180.0 + ZAZZZB
+ ZAZZZB 2 180.0
DVPREL1 13 PCOMP 4 24 -90.0 -270.0 + ZAZZZC
+ ZAZZZC 3 180.0
DVPREL1 14 PCOMP 4 28 -180.0 + ZAZZZD
+ ZAZZZD 4 180.0
DVPREL1 15 PCOMP 4 48 -180.0 + ZAZZZE
+ ZAZZZE 5 180.0
DVPREL1 16 PCOMP 4 54 -90.0 -270.0 + ZAZZZF
+ ZAZZZF 6 180.0
DVPREL1 17 PCOMP 4 58 -180.0 + ZAZZZG
+ ZAZZZG 7 180.0
DVPREL1 18 PCOMP 4 64 -225.0 + ZAZZZH
+ ZAZZZH 8 180.0
$ Define objective function (minimize Po)
DRESP2 100 Po 999 + ZZZZZI
+ ZZZZZI DESVAR 9
DEQATN 999 obj(Po)=Po
DEQATN 400000 f(Po,x,y)=10.0*LOG10((x*x+y*y)/(8.41e-18))/Po
$ Define system response locations
$ First window, port and starboard side
DRESP1 100000 AAAAAA FRDISP 1 12656
DRESP1 150000 IAAAAA FRDISP 7 12656
DRESP2 200000 BAAAAA 400000 + AAAAAA
+ AAAAAA DESVAR 9 + BAAAAA
+ BAAAAA DRESP1 100000 150000
DRESP1 100001 AAAAAAB FRDISP 1 12645
DRESP1 150001 IAAAAAB FRDISP 7 12645
DRESP2 200001 BAAAAAB 400000 + AAAAAAB
+ AAAAAAB DESVAR 9 + BAAAAAB
+ BAAAAAB DRESP1 100001 150001
$ Second window, port and starboard side
DRESP1 100002 AAAAAAC FRDISP 1 13611
DRESP1 150002 IAAAAAC FRDISP 7 13611
DRESP2 200002 BAAAAAC 400000 + AAAAAAC
+ AAAAAAC DESVAR 9 + BAAAAAC
+ BAAAAAC DRESP1 100002 150002
DRESP1 100003 AAAAAAD FRDISP 1 13738
DRESP1 150003 IAAAAAD FRDISP 7 13728
DRESP2 200003 BAAAAAD 400000 + AAAAAAD
+ AAAAAAD DESVAR 9 + BAAAAAD
+ BAAAAAD DRESP1 100003 150003
$ Third window, port and starboard side
DRESP1 100004 AAAAAAE FRDISP 1 14483
DRESP1 150004 IAAAAAE FRDISP 7 14483

```

```

DRESP2 200004 BAAAAE 400000 + AAAAAE
+ AAAAAE DESVAR 9 + BAAAAE
+ BAAAAE DRESP1 100004 150004
DRESP1 100005 AAAAAF FRDISP 1 14455
DRESP1 150005 IAAAAF FRDISP 7 14455
DRESP2 200005 BAAAAF 400000 + AAAAAF
+ AAAAAF DESVAR 9 + BAAAAF
+ BAAAAF DRESP1 100005 150005
$ Fourth window, port and starboard side
DRESP1 100006 AAAAAAG FRDISP 1 15352
DRESP1 150006 IAAAAAG FRDISP 7 15352
DRESP2 200006 BAAAAAG 400000 + AAAAAAG
+ AAAAAAG DESVAR 9 + BAAAAAG
+ BAAAAAG DRESP1 100006 150006
DRESP1 100007 AAAAAAH FRDISP 1 15454
DRESP1 150007 IAAAAAH FRDISP 7 15454
DRESP2 200007 BAAAAAH 400000 + AAAAAAH
+ AAAAAAH DESVAR 9 + BAAAAAH
+ BAAAAAH DRESP1 100007 150007
$ Fifth window, port and starboard side
DRESP1 100008 AAAAAI FRDISP 1 16404
DRESP1 150008 IAAAAI FRDISP 7 16404
DRESP2 200008 BAAAAI 400000 + AAAAAI
+ AAAAAI DESVAR 9 + BAAAAI
+ BAAAAI DRESP1 100008 150008
DRESP1 100009 AAAAAJ FRDISP 1 16410
DRESP1 150009 IAAAAJ FRDISP 7 16410
DRESP2 200009 BAAAAJ 400000 + AAAAAJ
+ AAAAAJ DESVAR 9 + BAAAAJ
+ BAAAAJ DRESP1 100009 150009
$ Define constraint cards on DRESP2 entries
DCONSTR 1 200000 1.0
DCONSTR 2 200001 1.0
DCONSTR 3 200002 1.0
DCONSTR 4 200003 1.0
DCONSTR 5 200004 1.0
DCONSTR 6 200005 1.0
DCONSTR 7 200006 1.0
DCONSTR 8 200007 1.0
DCONSTR 9 200008 1.0
DCONSTR 10 200009 1.0
DCONADD 500000 1 2 3 4 5 6 7 + ZZZZZZ
+ ZZZZZZ 8 9 10
DSCREEN EQUA -0.2
DOPTPRM DESMAX 11 P1 1 P2 15 + ZZZZZY
+ ZZZZZY DXMIN 0.075 DPMIN 0.10
INCLUDE 'structure.dat'
INCLUDE 'fluid.dat'

```